



# Intermediate Principal Stress Effects on the 3D Cracking Behavior of Flawed Rocks Under True Triaxial Compression

Yuan Sun<sup>1</sup> · Fan Fei<sup>2</sup> · Louis Ngai Yuen Wong<sup>3</sup> · Jinhyun Choo<sup>4</sup>

Received: 26 June 2023 / Accepted: 16 January 2024 / Published online: 6 March 2024  
© The Author(s) 2024

## Abstract

Crack initiation, growth, and coalescence in flawed rocks have been extensively studied for 2D (planar, penetrating) flaws under uniaxial/biaxial compression. However, little is known as to the mechanisms and processes of cracking from 3D flaws under true triaxial compression, where the intermediate principal stress ( $\sigma_2$ ) is distinguished from the major and minor principal stresses. In this work, we systematically investigate the effects of  $\sigma_2$  on the 3D cracking behavior of rock specimens with preexisting flaws, through the use of mechanistic simulations of mixed-mode fracture in rocks. We explore how two characteristics of  $\sigma_2$ , namely, (i) its orientation with respect to the flaw and (ii) its magnitude, affect two aspects of the cracking behavior, namely, (i) the cracking pattern and (ii) the peak stress. Results show that the orientation of  $\sigma_2$  exerts more control over the cracking pattern than the flaw inclination angle. The peak stress becomes highest when  $\sigma_1$  is parallel to the flaw, whereas it becomes lowest when  $\sigma_2$  is parallel to the flaw. Also, the effects of  $\sigma_2$  magnitude are more significant when  $\sigma_2$  becomes more oblique to the flaw plane. On the basis of our observations, we propose mechanisms underlying the cracking behavior of 3D flawed rocks under true triaxial compression.

## Highlights

- The effects of the intermediate principal stress ( $\sigma_2$ ) on the 3D cracking behavior of flawed rocks under true triaxial compression are systematically investigated.
- The orientation of  $\sigma_2$  exerts more control over the cracking pattern than the flaw inclination angle.
- The effects of  $\sigma_2$  magnitude become more significant when  $\sigma_2$  are more oblique to the flaw plane.
- Mechanisms underlying the cracking behavior of 3D flawed rocks under true triaxial compression are proposed based on the observations made.

**Keywords** Rock fracture · Intermediate principal stress · True triaxial condition · Numerical investigation · Phase-field modeling · Rock mass failure

✉ Jinhyun Choo  
jinhyun.choo@kaist.ac.kr

<sup>1</sup> Department of Civil Engineering, The University of Hong Kong, Pokfulam, Hong Kong

<sup>2</sup> Atmospheric, Earth, and Energy Division, Lawrence Livermore National Laboratory, Livermore, CA, USA

<sup>3</sup> Department of Earth Sciences, The University of Hong Kong, Pokfulam, Hong Kong

<sup>4</sup> Department of Civil and Environmental Engineering, KAIST, Daejeon, South Korea

## 1 Introduction

Rocks are heterogeneous brittle materials containing flaws across scales. These preexisting flaws are a source of stress concentration, which can in turn lead to crack initiation, growth, coalescence, and ultimately, material failure. Cracking from preexisting flaws is responsible for many rock failures observed in underground rock structures as well as natural rock masses.

Over the past decades, numerous studies have investigated how cracks nucleate, grow, interact, and coalesce from

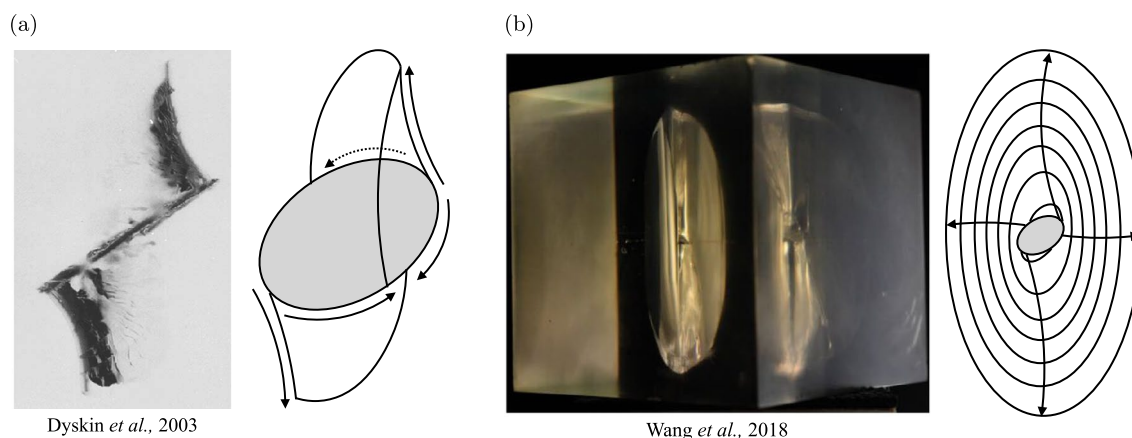


**Fig. 1** Experimentally observed effects of the intermediate principal stress on cracking patterns: **a** significant crack wrapping occurs when the specimen is under uniaxial compression (Dyskin et al. 2003),

whereas **b** cracking wrapping is absent when the specimen is under biaxial compression (Wang et al. 2018)

preexisting flaws in rocks and rock-like materials (e.g. Hoek and Bieniawski 1965; Bombolakis 1968; Cotterell 1972; Bobet and Einstein 1998b; Sagong and Bobet 2002; Park and Bobet 2009; Wong and Einstein 2009b, c, d; Lee and Jeon 2011; Morgan et al. 2013; Cheng et al. 2015; Zhang and Zhou 2022). Commonly, these studies have compressed specimens containing artificial flaws and observed the ensuing process of crack growth and coalescence. They have revealed a variety of cracking mechanisms (e.g. tensile crack, shear crack, and mixed-mode crack) and how they emerge differently according to the flaw configuration, material type, and other factors. A number of studies have also developed and used numerical models capable of reproducing the cracking processes observed in experiments (e.g. Ingraffea and Heuze 1980; Bobet and Einstein 1998a; Wu and Wong 2012; Zhang and Wong 2013; Ha et al. 2015; Lee et al. 2017; Bryant and Sun 2018; Fei and Choo 2021; Fei et al. 2021; Choo et al. 2023). The simulation results of these models have provided important insights that would be impossible to obtain by physical experiments alone.

While the majority of the existing studies have focused on flaws with 2D (planar, penetrating) geometry, 3D geometrical features are common in many flaws in practice (e.g. internally embedded flaws). As such, several studies have investigated cracking from 3D flaws in rock and rock-like materials, reporting some cracking patterns that do not arise from 2D flaws. For example, Yin et al. (2014) and Lu et al. (2015) have observed the development of petal cracks<sup>1</sup>

from 3D preexisting surface flaws as well as standard wing cracks. More recently, Zhou et al. (2018) studied how cracks develop from two cross-shaped flaws embedded in 3D specimens. They found a variety of substantial crack-wrapping patterns<sup>2</sup> under different conditions.

Still, however, most studies of 3D cracking processes have restricted their attention to a uniaxial stress condition in which the major principal stress ( $\sigma_1$ ) is only positive (compressive) and the other two principal stresses are absent. However, the stress states of rocks in the field are seldom uniaxial. Underground rocks are usually subjected to a true triaxial stress state in which  $\sigma_1 > \sigma_2 > \sigma_3 > 0$  ( $\sigma_2$  and  $\sigma_3$  denote the intermediate and minor principal stresses, respectively), and rocks at excavation boundaries are under a biaxial stress condition in which  $\sigma_1 > \sigma_2$  and  $\sigma_3 = 0$ . Also importantly, the intermediate principal stress determines the direction of fracture. It has also been shown that  $\sigma_2$  controls the angle of shear fracture or faulting (Haimson and Rudnicki 2010; Shalev and Lyakhovskiy 2018). A couple of recent studies have also revealed how the orientation and magnitude of  $\sigma_2$  affect the cracking behavior of rock specimens with 2D flaws (Zhang et al. 2020; Lu et al. 2021).

A few studies have demonstrated the importance of  $\sigma_2$  to 3D rock cracking by conducting biaxial compression tests on specimens containing internal flaws (e.g. Sahouryeh et al. 2002; Wang et al. 2018; Dyskin et al. 2003). They reported that the cracking patterns in the uniaxial and biaxial compression cases were completely different. Under uniaxial compression, significant crack wrapping occurred in the specimens and the wrapped cracks did not lead to splitting, see Fig. 1a. In contrast, under biaxial compression, such crack wrapping was not observed; instead, wing cracks propagated along the direction of  $\sigma_2$  until they split the specimens, as shown in Fig. 1b. Remarkably, the application of  $\sigma_2$  led to the localized failure of the specimens which

<sup>1</sup> A petal crack refers to a shell-like 3D tensile crack that initiates and propagates along the lateral edges of a preexisting 3D surface flaw.

<sup>2</sup> Crack wrapping refers to a specific crack pattern where the wing crack propagates along the circumference of a penny-shaped flaw until it forms a complete curved crack plane wrapping the flaw.

did not take place under uniaxial compression. As for the reason for this marked difference, the authors suggested that  $\sigma_2$  prevents crack wrapping and makes wing cracks grow in the direction parallel to  $\sigma_2$ . However, their tests of flawed specimens were limited to the case of  $\sigma_2 = \sigma_1$ , so it remains unclear how the effect of  $\sigma_2$  on 3D cracking manifests differently under various degrees of  $\sigma_2$ . Furthermore, as  $\sigma_3 = 0$  in biaxial tests, the effect of  $\sigma_2$  on 3D cracking has not been investigated under a true triaxial stress state, which is a more common stress condition of rocks *in situ*.

Although it has been found that both 3D geometry and  $\sigma_2$  play critical roles in the cracking behavior of rocks, little is known as to the mechanisms and processes of 3D cracking in rocks under a variety of  $\sigma_2$  conditions in true triaxial stress states Zhou et al. (2021a). This lack of knowledge may be attributed to the extreme difficulty of characterizing 3D cracking processes under true triaxial conditions. Past studies investigating cracking from flaws in rocks mainly used experimental approaches. They found that the use of a high-speed imaging system is essential to correctly identify the mechanisms and nature of cracks, as shear cracks often obscure preceding tensile wing cracks (Wong and Einstein 2009a). However, although a high-speed imaging system is readily applicable to uniaxial compression tests in which the lateral faces of the specimen are open, it cannot be applied to true triaxial tests in which all of the lateral faces are covered by loading systems. As an alternative means, computer simulations have been successfully utilized to investigate the mechanisms and processes of cracking from flaws in rocks, provided that the models faithfully incorporate the key characteristics of rock fracture and hence reproduce cracking processes as observed from experiments. However, the computer simulation of 3D cracking from flaws has been notoriously challenging, because it requires one not only to capture arbitrarily propagating fractures in 3D but also to distinguish their nature (*i.e.* tensile vs. shear).

The objective of the present work is to advance our understanding of 3D cracking from preexisting flaws in rocks in which  $\sigma_2$  is distinguished and varied. To this end, here we leverage the double-phase-field method (Fei and Choo 2021), a recently developed mechanistic model for mixed-mode fracture in rocks. The double-phase-field model is not only based on sound fracture mechanics principles (Barenblatt 1962; Dugdale 1960; Palmer and Rice 1973; Shen and Stephansson 1994), but it has also been validated against a wide range of experimental data on mixed-mode cracking in flawed rocks under compression (Fei and Choo 2021; Fei et al. 2021; Choo et al. 2023). Compared with other numerical methods for rock fracture simulations, the double-phase-field method has two standout features: (i) it does not require any algorithms for tracking crack geometry in 3D, and (ii) it naturally distinguishes between tensile and shear fractures. The combination of these two

features makes the double-phase-field method an ideal tool for investigating 3D cracking processes under true triaxial conditions. In this work, we validate the double-phase-field method against experimental data on 3D rock fracture and perform a systematic investigation into the effects of  $\sigma_2$  on the 3D cracking behavior of rock specimens with preexisting flaws. Specifically, we focus on elucidating how the orientation and magnitude of  $\sigma_2$  affect the cracking pattern and peak stress of rock specimens with an internally embedded flaw(s). Based on our observations, we propose mechanisms underlying the cracking behavior of 3D flawed rocks under true triaxial compression.

## 2 Methodology

In this section, we describe our methodology for investigating the effects of  $\sigma_2$  on the 3D cracking behavior of flawed rocks under true triaxial stress conditions. We begin by recapitulating the computational method employed for mechanistic simulations of mixed-mode fracture in rocks. We then validate the simulation method with two sets of experimental data in the literature. Finally, we design a series of numerical experiments to investigate the effects of  $\sigma_2$  in terms of its orientation and magnitude.

### 2.1 Simulation Method

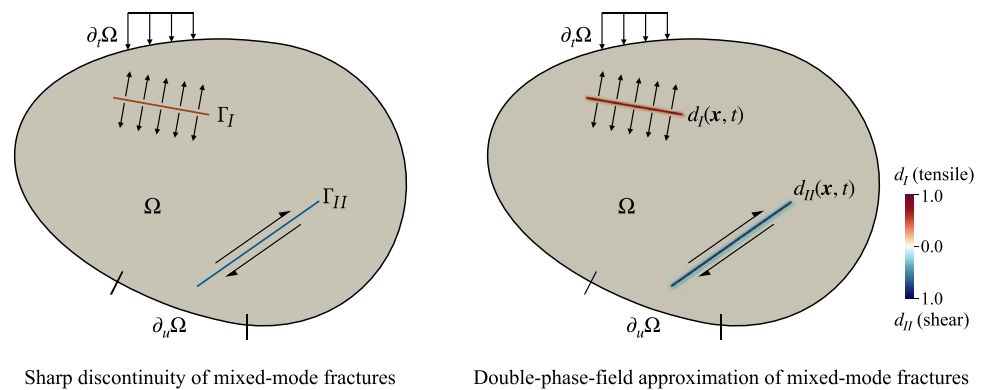
In this work, we make use of the double-phase-field method (Fei and Choo 2021) for mechanistic simulations of mixed-mode fracture in rocks. Among several other methods for the same purpose, the double-phase-field method is selected because it allows us to simulate and distinguish between tensile and shear fractures without any algorithms for geometry tracking. This feature is highly appealing for investigating complex mixed-mode fractures in 3D.

As illustrated in Fig. 2, the double-phase-field method diffusely approximates the discontinuous geometry of tensile and shear fractures by introducing two distinct phase fields, namely,  $d_I$  for tensile fracture, and  $d_{II}$  for shear fracture. The value of each phase field ranges from 0 to 1, where 0 represents an intact (undamaged) region and 1 represents a fully fractured region.

In the double-phase-field method, the mixed-mode fracturing process is simulated by the evolution of the two phase-fields. On the basis of fracture mechanics principles (Barenblatt 1962; Dugdale 1960; Palmer and Rice 1973; Shen and Stephansson 1994), the governing equations of the two phase fields can be derived as (see Fei and Choo 2021 for the detailed derivation):

$$-g'_I(d_I)\mathcal{H}_I - \frac{G_I}{\pi L}(2L^2 \nabla \cdot \nabla d_I - 2 + 2d_I) = 0, \quad (1)$$

**Fig. 2** Double-phase-field approximation of the discontinuous geometry of tensile (in red) and shear (in blue) fractures. After Fei and Choo (2021) (Color figure online)



$$-g'_{II}(d_{II})\mathcal{H}_{II} - \frac{\mathcal{G}_{II}}{\pi L}(2L^2 \nabla \cdot \nabla d_{II} - 2 + 2d_{II}) = 0. \quad (2)$$

Here,  $L$  is the length scale parameter determining the size of the phase-field approximation,  $\mathcal{G}_I$  and  $\mathcal{G}_{II}$  are the critical fracture energies for tensile and shear fractures, respectively;  $\mathcal{H}_I$  and  $\mathcal{H}_{II}$  are the crack driving forces for tensile and shear fractures, respectively; and  $g_I(d_I)$  and  $g_{II}(d_{II})$  are the degradation functions for tensile and shear fractures, respectively. The specific expressions for the crack driving forces and the degradation functions are presented in Appendix 1. The reader is referred to Fei and Choo (2021) for full details of the double-phase-field formulation and its derivation.

The double-phase-field method has a few features that set it apart from other phase-field models for fracture. First, it clearly distinguishes between tensile and shear fractures as they are represented by two different phase fields instead of a single phase field. Second, the double-phase-field model is formulated for *quasi-brittle* fracture rather than purely brittle fracture. The upshot of the quasi-brittle formulation is that the peak strength and softening behavior are not sensitive to the phase-field length parameter,  $L$ , allowing it to be regarded as a purely geometric parameter for phase-field regularization. This is not the case in the majority of existing phase-field models where  $L$  controls the strength and softening behavior and hence  $L$  should be “calibrated” despite its origin as a geometric regularization parameter (see *e.g.* Choo and Sun 2018a, b for discussions on this issue in the context of geomechanics). Third, in the double-phase-field model, the pressure dependence of frictional shear fracture and sliding is explicitly incorporated based on contact mechanics and fracture mechanics theory (Fei and Choo 2020a, b). Given these features, the double-phase-field method is ideally suited for this work.

The double-phase-field formulation can be numerically solved through a standard nonlinear finite element procedure. The details of the finite element procedure can be found in Fei and Choo (2021), and they are omitted for brevity. The numerical results in this paper are obtained with our

in-house code for geomechanics used in Choo (2019); Choo et al. (2021); Fei et al. (2022), which is built on the |deal.III finite element library (Arndt et al. 2019).

## 2.2 Validation of the Simulation Method

While the double-phase-field method has been validated against experimental data from compression tests on rock specimens with preexisting flaws (see Fei and Choo 2021; Fei et al. 2021 for details), the existing validations have been limited to cracking from 2D flaws under uniaxial compression. Meanwhile, as explained earlier, no experimental data is available for cracking from 3D flaws under true triaxial conditions. Therefore, here we validate the double-phase-field method against experimental data in two subsets of our problem of interest: (i) cracking from 2D flaws under true triaxial compression, and (ii) cracking from a 3D surface flaw under uniaxial compression.

### 2.2.1 Cracking from Two Coplanar 2D Flaws Under True Triaxial Compression

First, we validate the double-phase-field method for cracking behavior under true triaxial compression. For this purpose, we simulate a true triaxial compression test that Zhou et al. (2021b) conducted on a fine sandstone specimen with two coplanar 2D flaws. The experimental setup is depicted in Fig. 3a. The specimen is a 100-mm-long cube containing two coplanar, fully-penetrating flaws. Each flaw is 1 mm wide, 16 mm long with a ligament length of 8 mm, and inclined 45° from the horizontal. The true triaxial loading path applied to the specimen is depicted in Fig. 3b.

Table 1 lists the material parameters used for simulating the experiment. For those measured in Zhou et al. (2021b), we adopt their values directly. For those not measured, namely Young’s modulus ( $E$ ) and the Mode I and II fracture energies ( $\mathcal{G}_I$  and  $\mathcal{G}_{II}$ ), we calibrate them based on the stress–strain data in Zhou et al. (2021b). Particularly, to calibrate the fracture energies, we first set the reasonable

**Fig. 3** Cracking from two coplanar 2D flaws under true triaxial compression: experimental setup (Zhou et al. 2021b). **a** Specimen geometry. **b** Loading scheme

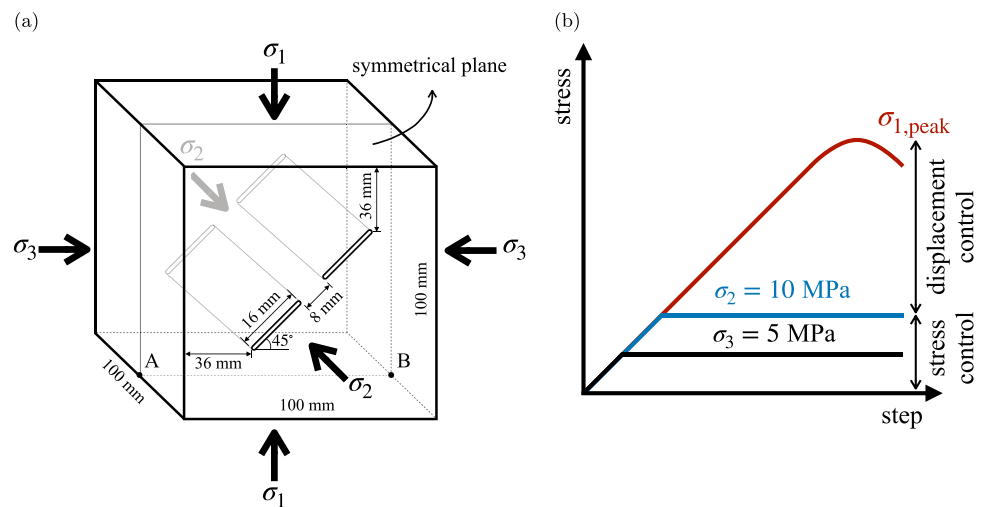


**Table 1** Cracking from two coplanar 2D flaws under true triaxial compression: material parameters

Parameter	Symbol	Unit	Value	References
Young's modulus	$E$	GPa	6.363	Calibrated from Zhou et al. (2021b)
Poisson ratio	$\nu$	–	0.189	Measured in Zhou et al. (2021b)
Tensile strength	$\sigma_t$	MPa	5.75	Measured in Zhou et al. (2021b)
Cohesion	$c$	MPa	17.44	Measured in Zhou et al. (2021b)
Peak friction angle	$\phi_p$	deg	38.9	Measured in Zhou et al. (2021b)
Residual friction angle	$\phi_r$	deg	38.9	Measured in Zhou et al. (2021b)
Mode I fracture energy	$\mathcal{G}_I$	J/m <sup>2</sup>	98	Calibrated from Zhou et al. (2021b)
Mode II fracture energy	$\mathcal{G}_{II}$	J/m <sup>2</sup>	1500	Calibrated from Zhou et al. (2021b)

ranges of their values in rocks according to data in the literature (Shen and Stephansson 1994; Bažant and Kazemi 1990). Then, within the ranges, we determine the values of the fracture energies that make the simulated peak stress closest to the experimentally measured one. It is confirmed that the ratio of the fracture energies,  $\mathcal{G}_I/\mathcal{G}_{II}$ , falls within its typical range for rocks.

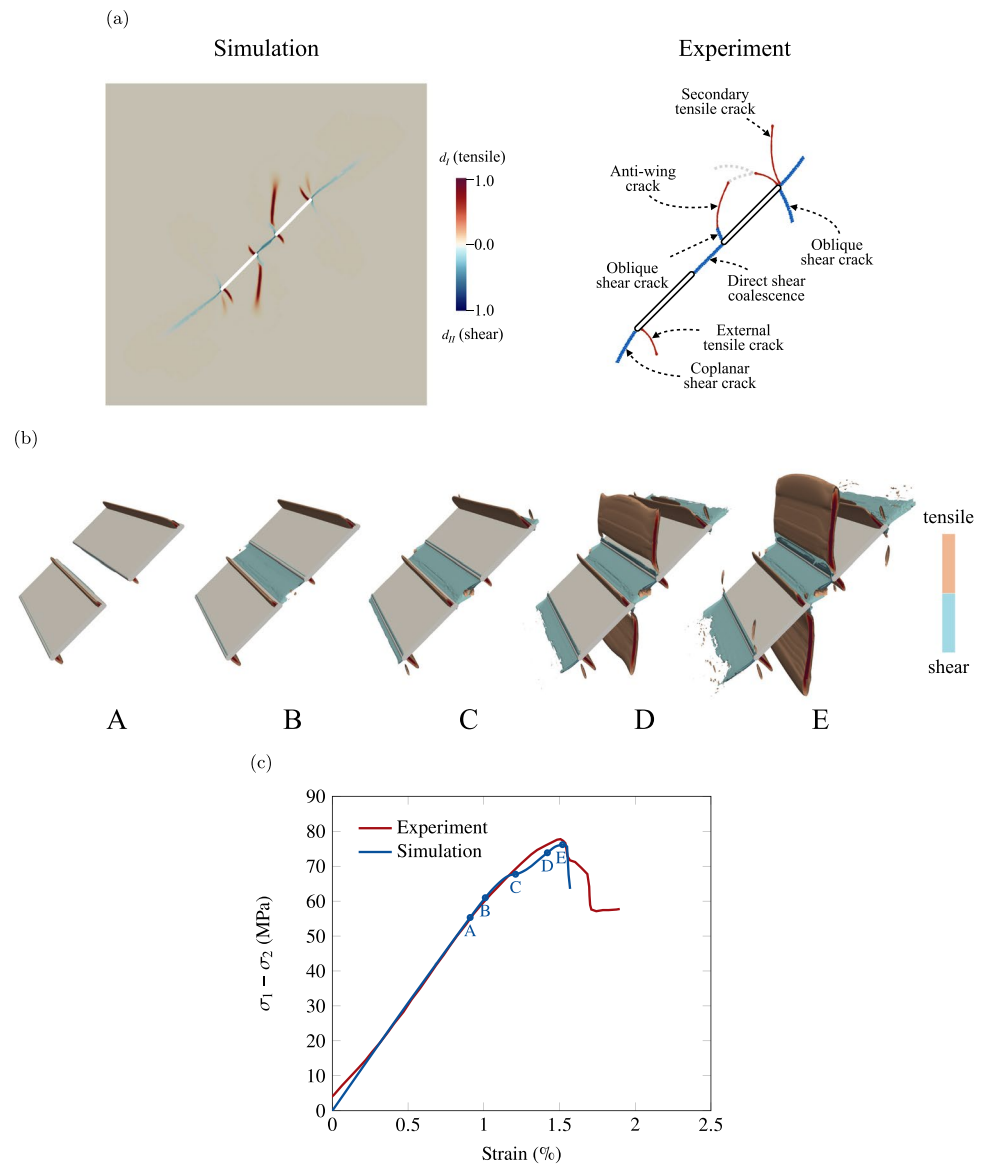
Taking advantage of symmetry, we model half of the specimen. We set the phase-field length parameter as  $L = 0.3$  mm and refine elements near the flaw such that the element size  $h$  satisfies  $L/h \geq 2$ , which results in around 5,500,000 hexahedral elements. From a mesh sensitivity study described in Appendix 2, we confirm that the simulation results show little dependence on the mesh as long as  $L/h \geq 2$ . We then apply the true triaxial loading scheme depicted in Fig. 3b, increasing the boundary tractions with an increment of 0.5 MPa until they reach the prescribed values. During this stress-controlled loading stage, Points A and B on the bottom surfaces are fixed for stability. Then, in the final stage where  $\sigma_1$  is controlled by the displacement, we

apply a displacement increment of  $1 \times 10^{-2}$  mm on the top surface, while fixing the bottom surface by rollers.

Figure 4 compares the simulation and experimental results on cracking from two coplanar 2D flaws under true triaxial compression. As can be seen from Fig. 4a, the cracking pattern in the simulation is consistent with the experimental observation in terms of the crack type, crack geometry and crack coalescence pattern. Specifically, as shown in Fig. 4b, external tensile cracks and secondary tensile cracks first nucleate from the outer tips of the flaws, followed by the development of oblique shear cracks from both the inner and outer tips of the flaws. Anti-wing cracks grow from the shear crack fronts toward the  $\sigma_1$  loading direction. The flaws directly coalesce through a shear crack, and coplanar shear cracks initiate from the outer tips of the flaws and grow along the flaw planes. Besides this agreement in cracking patterns, the stress–strain curves in Fig. 4c also match remarkably well. Thus it has been validated that the double-phase-field model can well reproduce cracking processes under true triaxial compression, in both qualitative and quantitative manners.



**Fig. 4** Cracking from two coplanar 2D flaws under true triaxial compression. **a** Simulated cracking patterns at the peak stress and experimentally observed cracking patterns at the ultimate failure state. **b** Evolution of 3D mixed-mode cracks in the simulation. **c** Stress–strain curves from the simulation and experiments. The experimental results are redrawn from Zhou et al. (2021b). (The experimental stress–strain curve is redrawn excluding the initial nonlinear portion related to the closure of preexisting defects at the microscale.)



### 2.2.2 Cracking from a 3D Surface Flaw Under Uniaxial Compression

As our second validation problem, we consider the uniaxial compression tests of Lu et al. (2015) on red sandstone specimens with a 3D surface flaw. Figure 5 shows the setup of the experiments. Each specimen is 70 mm wide, 20 mm long, and 120 mm high, and it contains a surface flaw that is semi-elliptic, 30 mm long, 0.65 mm wide, and inclined  $45^\circ$  from the horizontal. We consider two cases with different flaw depths,  $a = 8$  mm and 12 mm.

Table 2 presents the material parameters used in the example. The elasticity parameters ( $E$  and  $\nu$ ) and the cohesion ( $c$ ) are directly adopted from the experiments (Lu et al. 2015). However, the tensile strength ( $\sigma_t$ ) and the peak and residual friction angles ( $\phi_p$  and  $\phi_r$ ) are unavailable from

the experiments. So we adopt their values from other tests on red sandstone specimens (Yang et al. 2012; Zhang et al. 2021). The Mode I and Mode II fracture energies ( $\mathcal{G}_I$  and  $\mathcal{G}_{II}$ ) are calibrated to match the peak stresses measured in the experiments. The calibrated values and their mode mixity ratio ( $\mathcal{G}_I/\mathcal{G}_{II}$ ) are within their ranges for real rocks (Shen and Stephansson 1994; Hou et al. 2021; Nejati et al. 2021).

For numerical simulation, we set the phase-field length parameter as  $L = 0.4$  mm and discretize the domain in the same way as the previous problem. As a result, the domain is discretized by approximately 4,400,000 hexahedral elements (the specific element number depends on the flaw depth). Regarding boundary conditions, the bottom surface is supported by rollers, and Points A and B in Fig. 5 are further constrained by pins for stability. Uniaxial loading is uniformly applied on the top surface with a displacement

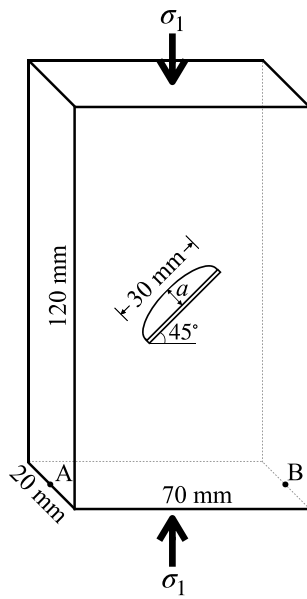


**Fig. 5** Cracking from a 3D surface flaw under uniaxial compression: experimental setup Lu et al. (2015)

increment of  $2 \times 10^{-3}$  mm. The lateral surfaces are traction-free.

Figure 6 compares the simulation and experimental results when the flaw depth  $a$  is 8 mm. It is noted that when the experimental results of Lu et al. (2015) were redrawn, far-field cracks were excluded as they developed during unstable rupture, which is beyond the scope of this study. As shown in Fig. 6a, the double-phase-field method can reproduce the cracking patterns on the surface and different sections observed from the experiment. In Fig. 6b, we also show how 3D mixed-mode cracks develop from the flaw and evolve until the peak stress, at the strains marked in Fig. 6c. From Fig. 6c, one can also see that the simulated stress–strain curve is similar to the experimental data.

In Fig. 7 we compare the simulation and experimental results for the case of  $a = 12$  mm. It can be seen from Fig. 7a that the simulated cracking patterns are again close to the experimental results. The evolution of 3D mixed-mode

cracks in this case is presented in Fig. 7b. The stress–strain curves in Fig. 7c also show good agreement. These results validate that the double-phase-field model can faithfully simulate cracking processes from a 3D flaw.

### 2.3 Design of Numerical Experiments

Having validated our simulation method, we now design a series of numerical experiments to systematically investigate the effects of  $\sigma_2$  on rock specimens with a preexisting 3D flaw(s). To this end, we draw on the setup of the first validation example (*cf.* Fig. 3), modifying the 2D flaws with 3D internal flaw(s). Other factors such as the specimen size, the loading scheme, and material parameters remain unchanged.

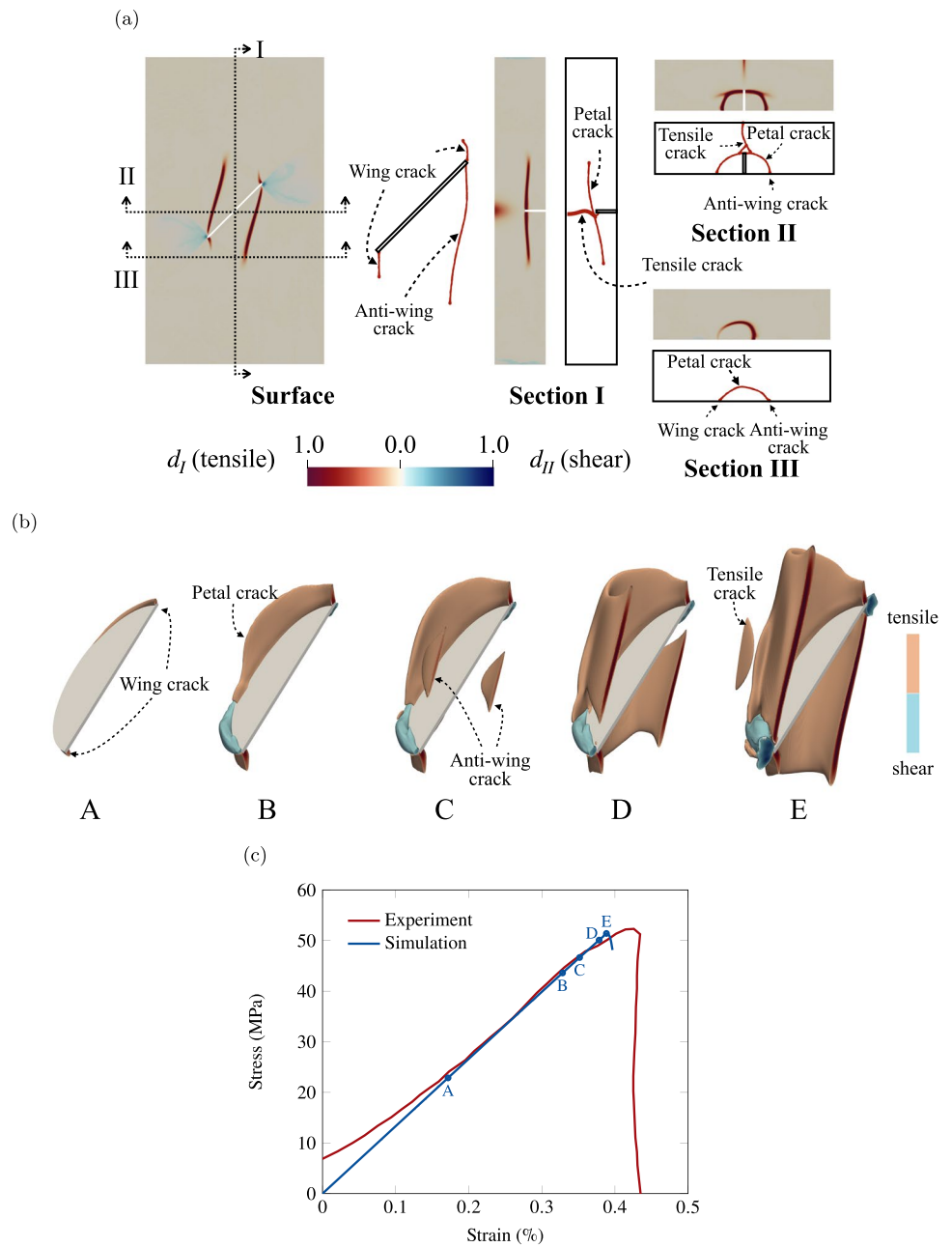
Figure 8 illustrates the geometry of specimens with single or double internal flaws. These internal flaws are cylinders with a diameter of 16 mm and a width of 1 mm, and the flaw planes are parallel to the  $y$  direction. In the single-flawed specimen, the internal flaw is located at the center of the specimen. The minimum distance between the flaw edge and specimen surfaces is 42 mm. In the double-flawed specimens, the internal flaws are coplanar with a ligament length of 8 mm located at the center of the specimen. The minimum distance between the flaw edge and specimen surfaces is around 31–36 mm. (The specific distance depends on the flaw inclination angle).

In this work, we investigate the effects of  $\sigma_2$  in two aspects: (i) its orientation with respect to the flaw(s), and (ii) its magnitude. To study the effects of  $\sigma_2$  orientation, we adopt the same  $\sigma_2$  and  $\sigma_3$  (10 MPa and 5 MPa, respectively) from the validation experiment. Under these constant  $\sigma_2$  and  $\sigma_3$ , we consider three cases of principal stress orientations (i)  $\sigma_2 - \sigma_1 - \sigma_3$ , (ii)  $\sigma_3 - \sigma_1 - \sigma_2$ , and (iii)  $\sigma_1 - \sigma_2 - \sigma_3$  (written in the sequence of  $\sigma_x - \sigma_y - \sigma_z$  defined in Fig. 8.) To study the effects of  $\sigma_2$  magnitude, we consider six levels of  $\sigma_2$  to cover the entire range from  $\sigma_2 = \sigma_3$  to  $\sigma_2 = \sigma_1$ : 5, 10, 20, 40, 80 MPa, and  $\sigma_{1,\text{peak}}$ . (In all cases,  $\sigma_3 = 5$  MPa as in the validation experiment.) Table 3 summarizes the details of the parameter studies.

**Table 2** Cracking from a 3D surface flaw under uniaxial compression: material parameters

Parameter	Symbol	Unit	Value	References
Young's modulus	$E$	GPa	13.5	Measured in Lu et al. (2015)
Poisson ratio	$\nu$	–	0.26	Measured in Lu et al. (2015)
Tensile strength	$\sigma_t$	MPa	3.28	Measured in Zhang et al. (2021)
Cohesion	$c$	MPa	16.2	Measured in Lu et al. (2015)
Peak friction angle	$\phi_p$	deg	35	Measured in Yang et al. (2012)
Residual friction angle	$\phi_r$	deg	32	Measured in Yang et al. (2012)
Mode I fracture energy	$\mathcal{G}_I$	J/m <sup>2</sup>	18	Calibrated from Lu et al. (2015)
Mode II fracture energy	$\mathcal{G}_{II}$	J/m <sup>2</sup>	130	Calibrated from Lu et al. (2015)

**Fig. 6** Cracking from a 3D surface flaw under uniaxial compression: flaw depth  $a = 8$  mm. **a** Simulated cracking patterns at the peak stress and experimentally observed cracking patterns at the ultimate failure state. **b** Evolution of 3D mixed-mode cracks in the simulation. **c** Stress–strain curves from the simulation and experiments. The experimental results are redrawn from Lu et al. (2015). (The experimental stress–strain curve is redrawn excluding the initial nonlinear portion related to the closure of preexisting defects at the microscale.)



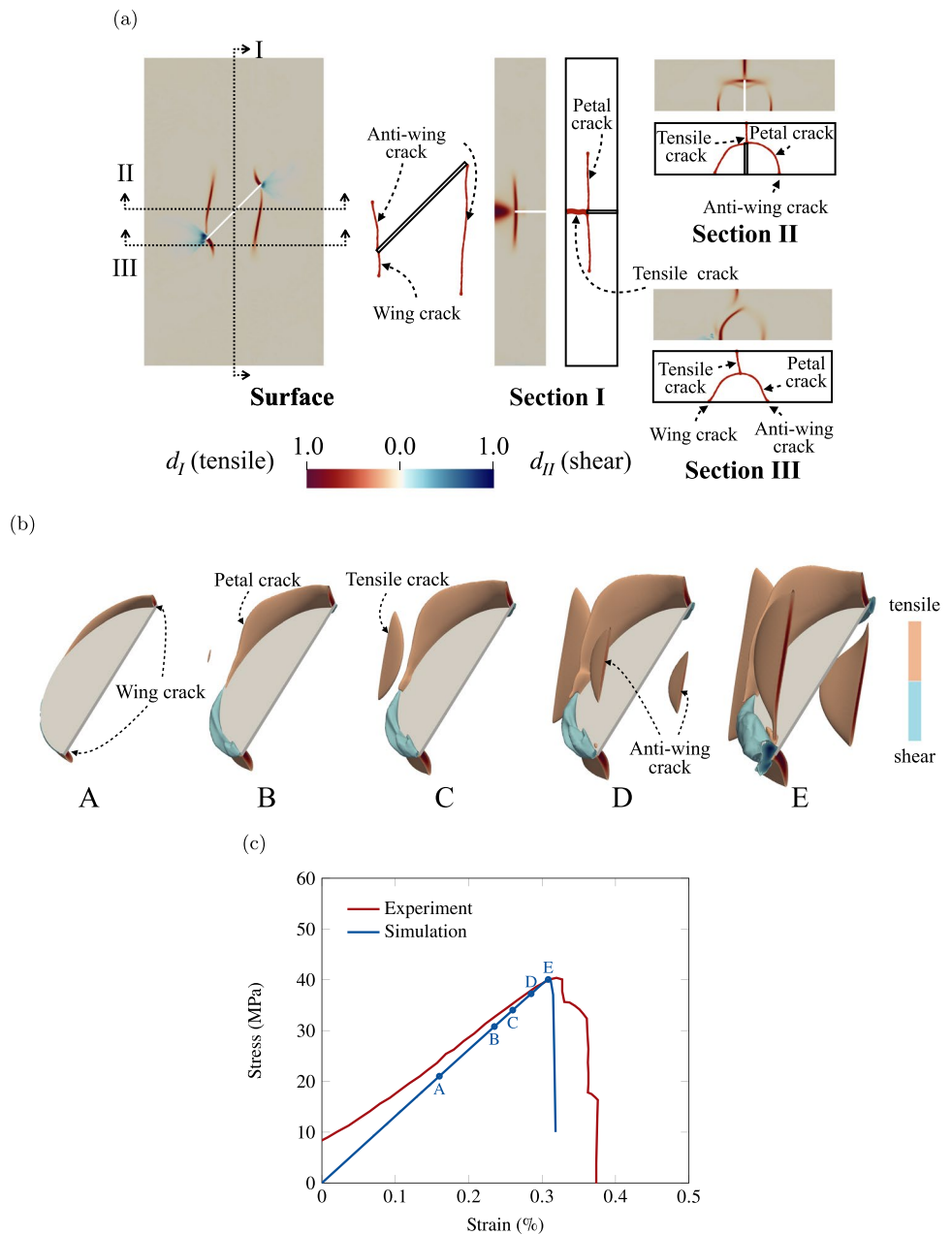
In the following sections, we investigate how the orientation and magnitude of  $\sigma_2$  affect two aspects of cracking behavior: (i) the cracking pattern and (ii) peak stress. Without ambiguity, we shall refer to the crack morphology at the onset of failure (*i.e.* when  $\sigma_1$  reaches its peak) as the cracking pattern. Also, for the sake of visualizing 3D internal cracks, we define tensile cracks as regions where  $d_I \geq 0.2$  and shear cracks as regions where  $d_{II} \geq 0.2$ .

### 3 Effects of the Orientation of the Intermediate Principal stress

In this section, we examine how the *orientation* of  $\sigma_2$  affects the cracking patterns and peak stresses in the single- and double-flawed specimens. To this end, we shall compare the simulation results in the following three cases: (i) when  $\sigma_2$  is parallel to the flaw plane, (ii) when  $\sigma_2$  is oblique to the flaw plane and  $\sigma_3$  is parallel to the flaw plane, and (iii) when  $\sigma_2$  is oblique to the flaw plane and  $\sigma_1$  is parallel to the flaw plane. For a brief distinction between the latter two cases where  $\sigma_2$



**Fig. 7** Cracking from a 3D surface flaw under uniaxial compression: flaw depth  $a = 12$  mm. **a** Simulated cracking patterns at the peak stress and experimentally observed cracking patterns at the ultimate failure state. **b** Evolution of 3D mixed-mode cracks in the simulation. **c** Stress–strain curves from the simulation and experiments. The experimental results are redrawn from Lu et al. (2015). (The experimental stress–strain curve is redrawn excluding the initial nonlinear portion related to the closure of preexisting defects at the microscale.)



is oblique to the flaw plane, we shall refer to them with the principal stress that is parallel to the flaw plane.

### 3.1 Cracking Patterns

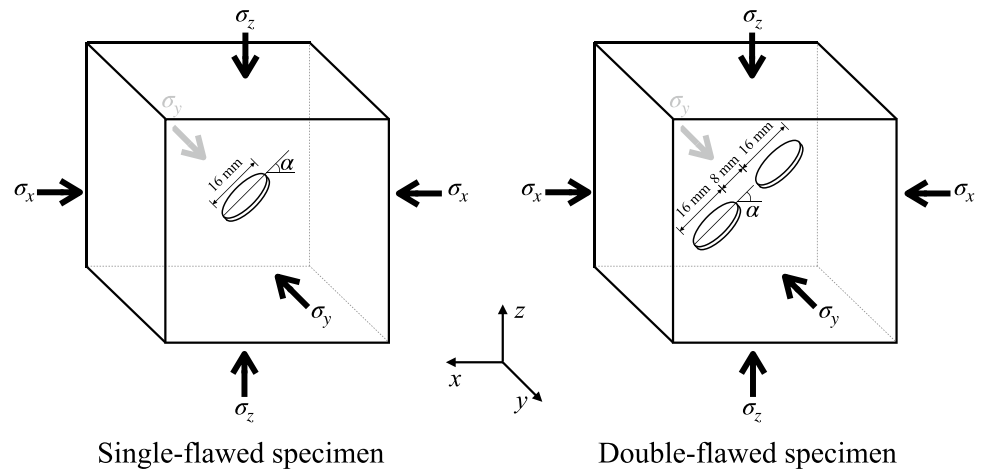
#### 3.1.1 Single Internal Flaw

Figure 9 presents the cracking patterns in the specimen containing the flaw with  $\alpha = 45^\circ$ , under three different cases of principal stress orientations. The results show that the orientation of principal stresses has a significant impact on the crack patterns. When  $\sigma_2$  is parallel to the flaw plane (Fig. 9a), tensile wing cracks initiate from the upper and lower flaw

tips, and a pair of planar shear cracks grow from the tensile crack fronts in the flaw direction. On the other hand, when  $\sigma_3$  is parallel to the flaw plane (Fig. 9b), tensile wing cracks initiate from the flaw edge, and other types of tensile cracks—called fish-fin cracks in the literature (Adams and Sines 1978)—emerge from the flaw center along the symmetrical plane. Meanwhile, several conjugate pairs of shear cracks develop from the flaw. Lastly, when  $\sigma_1$  is parallel to the flaw plane (Fig. 9c), almost no tensile cracks develop, while two conjugate pairs of shear cracks grow from the flaw surfaces.

Despite the apparent differences in the crack patterns, there exist common mechanisms underlying the cracking

**Fig. 8** Cracking from single and double internal flaws under true triaxial compression: setup of numerical experiments



**Table 3** Descriptions of the two numerical experiments in this work. (Note that  $\sigma_3 = 5$  MPa in all cases.)

Case	Purpose	Number of internal flaws	Flaw inclination angle ( $\alpha$ )	$\sigma_2$ orientation ( $\sigma_x - \sigma_y - \sigma_z$ )	$\sigma_2$ magnitude (MPa)
1	To study the effects of $\sigma_2$ orientation	Single & Double	$15^\circ, 45^\circ, 75^\circ$	$\sigma_3 - \sigma_2 - \sigma_1$ $\sigma_2 - \sigma_3 - \sigma_1$ $\sigma_3 - \sigma_1 - \sigma_2$	10
2	To study the effects of $\sigma_2$ magnitude	Single & Double	$45^\circ$	$\sigma_3 - \sigma_2 - \sigma_1$ $\sigma_2 - \sigma_3 - \sigma_1$ $\sigma_3 - \sigma_1 - \sigma_2$	$5(= \sigma_3), 10, 20, 40, 80, \sigma_{1,peak}$

pattern. First, tensile cracks propagate on the  $\sigma_1 - \sigma_2$  plane. This mechanism, which is consistent with the experimental observations in the literature (e.g. Sahouryeh et al. 2002; Wang et al. 2018; Lu et al. 2021), can be explained by that the tensile hoop stress is maximum on the  $\sigma_1 - \sigma_2$  plane. When  $\sigma_1$  is parallel to the flaw plane, however, the maximum tensile hoop stress is not high enough to trigger tensile cracks, and hence tensile cracks do not develop. Second, shear cracks propagate in the path that lies on the  $\sigma_1 - \sigma_3$  plane, being inclined to the  $\sigma_1$  direction with acute angles. This is consistent with the experimental data of Zhou et al. (2021b) and Zhang et al. (2023a), and it can be attributed to that the shear stress is maximum on the  $\sigma_1 - \sigma_3$  plane. As a result, when  $\sigma_2$  is parallel to the flaw plane, shear cracks propagate parallel to the flaw plane. It would be worth noting that the resulting shear failure zone looks similar to those developed in intact rock specimens under true triaxial compression (Ma and Haimson 2016; Ma et al. 2017; Zhang et al. 2023b). However, when  $\sigma_2$  is oblique to the flaw plane, shear cracks develop in directions different from the flaw plane.

Figures 10 and 11 show the cracking patterns when the flaw angle becomes changed to  $\alpha = 15^\circ$  and  $\alpha = 75^\circ$ , respectively. It can be seen that the flaw inclination angle has some

minor influence. For example, when  $\sigma_1$  is more normal to the flaw plane, the maximum hoop stress on the  $\sigma_1 - \sigma_2$  plane becomes larger, and so more tensile cracks develop. This observation is in agreement with the experimental findings of Zhang et al. (2023a). But the overall cracking patterns are more or less the same as those in the  $\alpha = 45^\circ$  case. This similarity indicates that the patterns of cracking from a single flaw are mainly dominated by the orientation of principal stresses rather than the flaw inclination angle.

### 3.1.2 Double Internal Flaws

In Fig. 12 we examine the cracking patterns in the specimen with two internal flaws of  $\alpha = 45^\circ$ . Our focus here is how the crack coalescence—absent in the single-flawed specimens discussed previously—is affected by the orientation of principal stresses. When  $\sigma_2$  is parallel to the flaw plane (Fig. 12a), the two flaws coalesce through mixed-mode cracks. When  $\sigma_3$  is parallel to the flaw plane (Fig. 12b), the two flaws coalesce through shear cracks. When  $\sigma_1$  is parallel to the flaw plane (Fig. 12c), the two flaws do not coalesce. These results consistently indicate that the patterns of crack coalescence change according to how tensile and

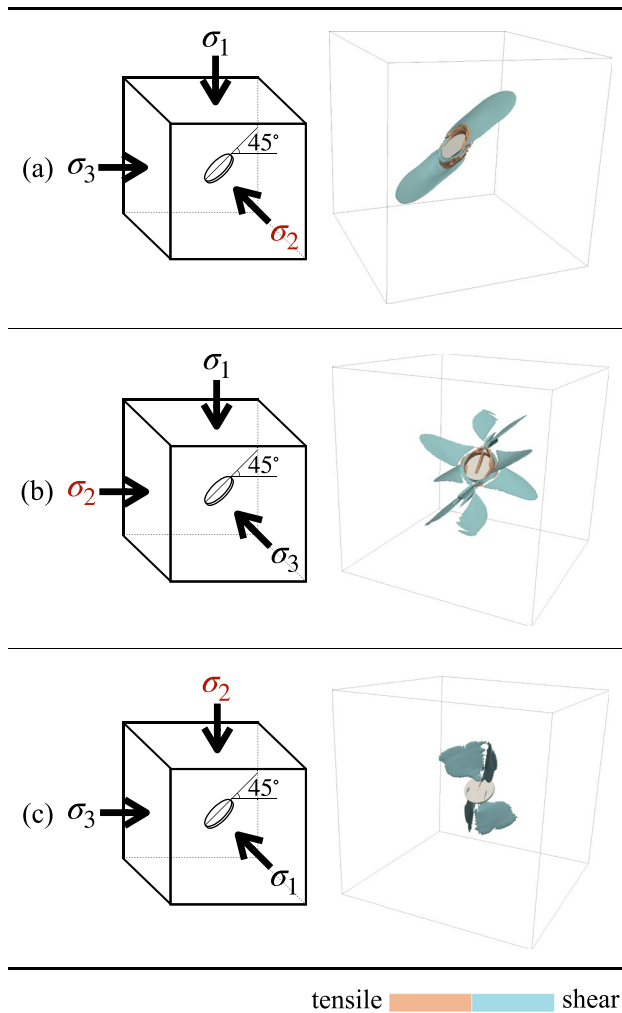


**Fig. 9** Cracking patterns in the single-flawed specimen with  $\alpha = 45^\circ$ . **a**  $\sigma_2$  is parallel to the flaw plane. **b**  $\sigma_3$  is parallel to the flaw plane. **c**  $\sigma_1$  is parallel to the flaw plane

shear cracks are affected by the orientations of  $\sigma_2$  and other principal stresses.

Figures 13 and 14 show the cracking patterns when the flaw inclination angle becomes  $\alpha = 15^\circ$  and  $\alpha = 75^\circ$ , respectively. As in the previous case, the two flaws coalesce through mixed-mode cracks when  $\sigma_2$  is parallel to the flaw plane (Figs. 13a and 14a), and they do not coalesce when  $\sigma_2$  is oblique to the flaw plane and  $\sigma_1$  is parallel to the flaw plane (Figs. 13c and 14c). In these two cases, the flaw angle has little influence on the crack coalescence. However, when  $\sigma_2$  is oblique to the flaw plane and  $\sigma_3$  is parallel to the flaw plane (Figs. 13b and 14b), the flaw angle exerts dominant control over the crack coalescence. When  $\alpha = 15^\circ$  (Fig. 13b), the two flaws still coalesce through shear cracks like the previous case of  $\alpha = 45^\circ$ ; however, when  $\alpha = 75^\circ$  (Fig. 14b), the two flaws no longer coalesce. These results suggest that the

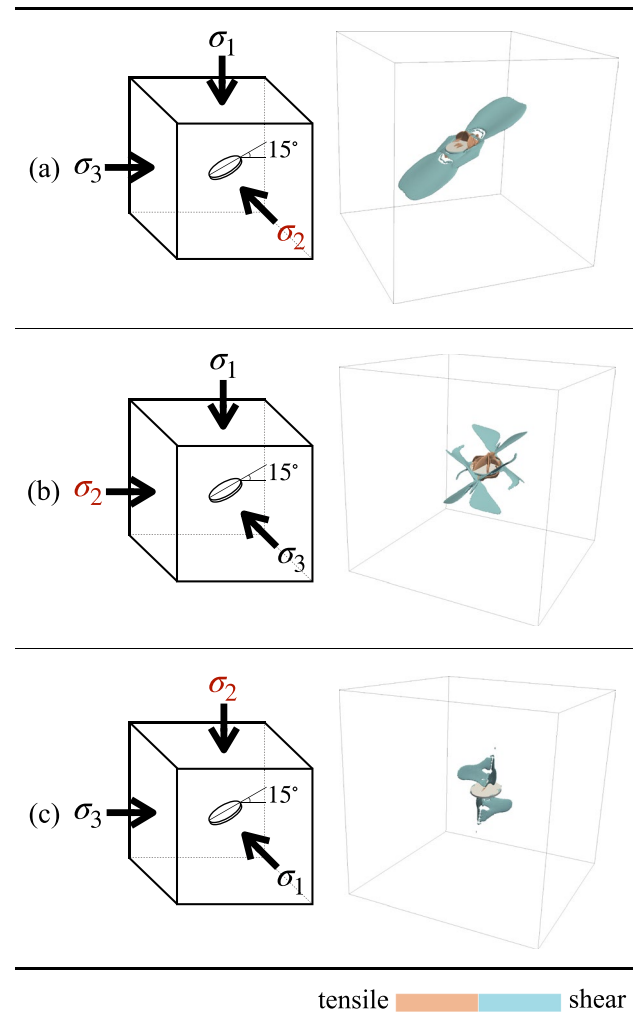


**Fig. 10** Cracking patterns in the single-flawed specimen with  $\alpha = 15^\circ$ . **a**  $\sigma_2$  is parallel to the flaw plane. **b**  $\sigma_3$  is parallel to the flaw plane. **c**  $\sigma_1$  is parallel to the flaw plane

flaw inclination angle may have a significant impact on the coalescence of preexisting flaws under certain conditions.

### 3.2 Peak Stresses

Turning our attention to the peak stress (*i.e.* the magnitude of  $\sigma_1$  at failure), in Fig. 15 we compare the peak stresses in the single- and double-flawed specimens. It can be seen that for a given inclination angle, the peak stress is highest when  $\sigma_1$  is parallel to the flaw plane, while it is lowest when  $\sigma_2$  is parallel to the flaw plane. This trend is consistent with the experimental observation by Lu et al. (2021), where peak stresses are lower when  $\sigma_2$  is parallel to the flaw plane. Also, except when  $\sigma_1$  is parallel to the flaw, the peak stress generally decreases as the inclination angle becomes lower. This variation is also consistent with how the peak stress in

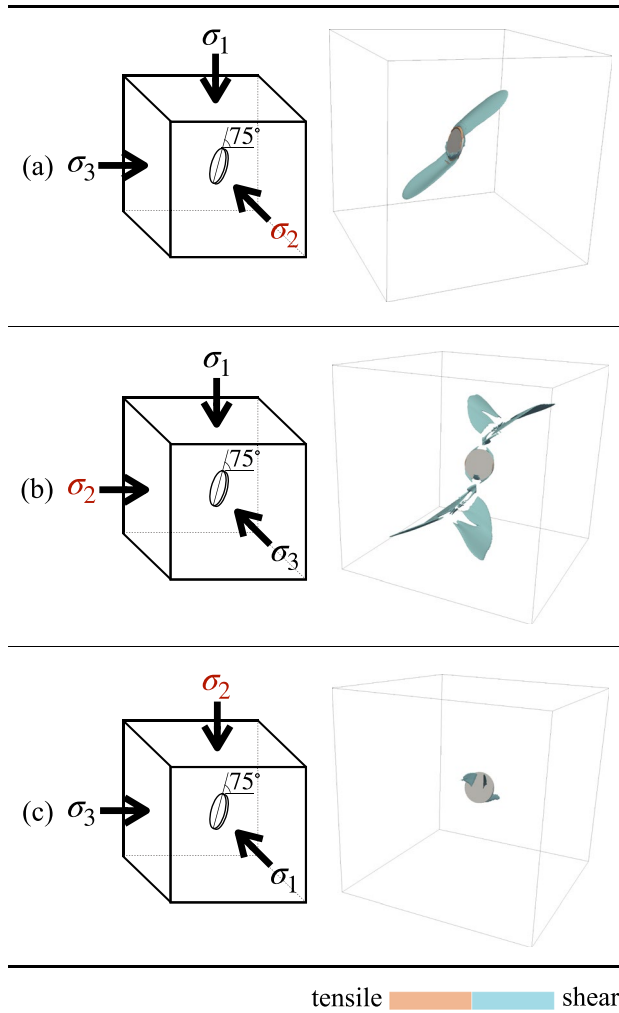


**Fig. 11** Cracking patterns in the single-flawed specimen with  $\alpha = 75^\circ$  under different  $\sigma_2$  orientations. **a**  $\sigma_2$  is parallel to the flaw plane. **b**  $\sigma_3$  is parallel to the flaw plane. **c**  $\sigma_1$  is parallel to the flaw plane

flawed rocks under uniaxial compression changes with the flaw angle (Lee and Jeon 2011). It is also noted that, as the flaw inclination angle changes, the degree of the effect of  $\sigma_2$  orientation becomes different. Specifically, the effect of the  $\sigma_2$  orientation becomes greater as the flaw inclination angle becomes lower.

The variations in the peak stress with the principal stress orientations can be related to how the cracking patterns change. When  $\sigma_2$  is parallel to the flaw plane, planar shear cracks develop along the flaw plane. Since the flaw is a weak zone, the strengths of a flawed specimen must be lowest when it fails along the flaw plane. Meanwhile, when  $\sigma_1$  is parallel to the flaw plane, the number of developed cracks

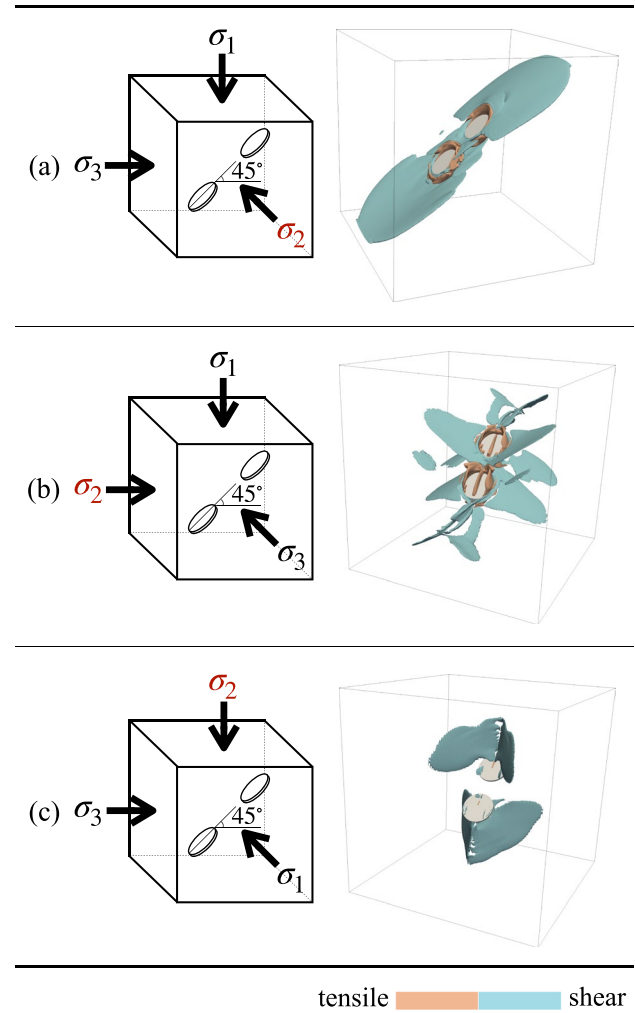


**Fig. 12** Cracking patterns in the double-flawed specimen with  $\alpha = 45^\circ$ . **a**  $\sigma_2$  is parallel to the flaw plane. **b**  $\sigma_3$  is parallel to the flaw plane. **c**  $\sigma_1$  is parallel to the flaw plane

is the smallest, and hence the strength is higher than the other cases.

#### 4 Effects of the Magnitude of the Intermediate Principal Stress

In this section, we investigate how the *magnitude* of  $\sigma_2$  controls the cracking patterns and peak stresses under different orientations of principal stresses. Depending on the relative magnitude of  $\sigma_2$  with respect to  $\sigma_1$  and  $\sigma_3$ , we shall classify the loading conditions into three regimes: (i) triaxial compression ( $\sigma_1 > \sigma_2 = \sigma_3$ ), (ii) true triaxial compression ( $\sigma_1 > \sigma_2 > \sigma_3$ ); and (iii) triaxial extension ( $\sigma_1 = \sigma_2 > \sigma_3$ ).

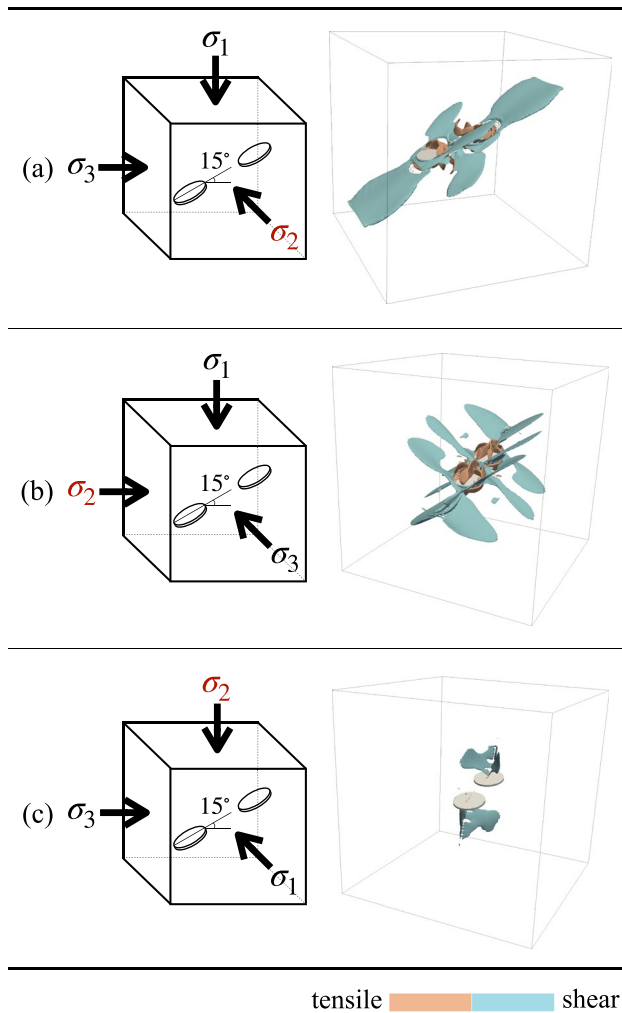


**Fig. 13** Cracking patterns in the double-flawed specimen with  $\alpha = 15^\circ$ . **a**  $\sigma_2$  is parallel to the flaw plane. **b**  $\sigma_2$  is oblique to the flaw plane and  $\sigma_3$  is parallel to the flaw plane. **c**  $\sigma_2$  is oblique to the flaw plane and  $\sigma_1$  is parallel to the flaw plane

## 4.1 Cracking Patterns

### 4.1.1 Single Internal Flaw

Figure 16 presents the cracking patterns (crack morphology at failure) in true triaxial tests conducted with different magnitudes of  $\sigma_2$ , in case  $\sigma_2$  is parallel to the flaw. To better illustrate the transition of the cracking patterns, the figure also includes the Mode-I and Mode-II phase-field values in two sections: one parallel to the  $\sigma_1 - \sigma_3$  plane and the other parallel to the  $\sigma_1 - \sigma_2$  plane. The results show that when  $\sigma_2$  is equal to  $\sigma_3$  (triaxial compression), wrapping cracks develop. However, when  $\sigma_2$  is greater than  $\sigma_3$  (true triaxial compression), localized shear cracks grow without wrapping. This difference is similar to how cracking patterns in 3D flawed specimens are different

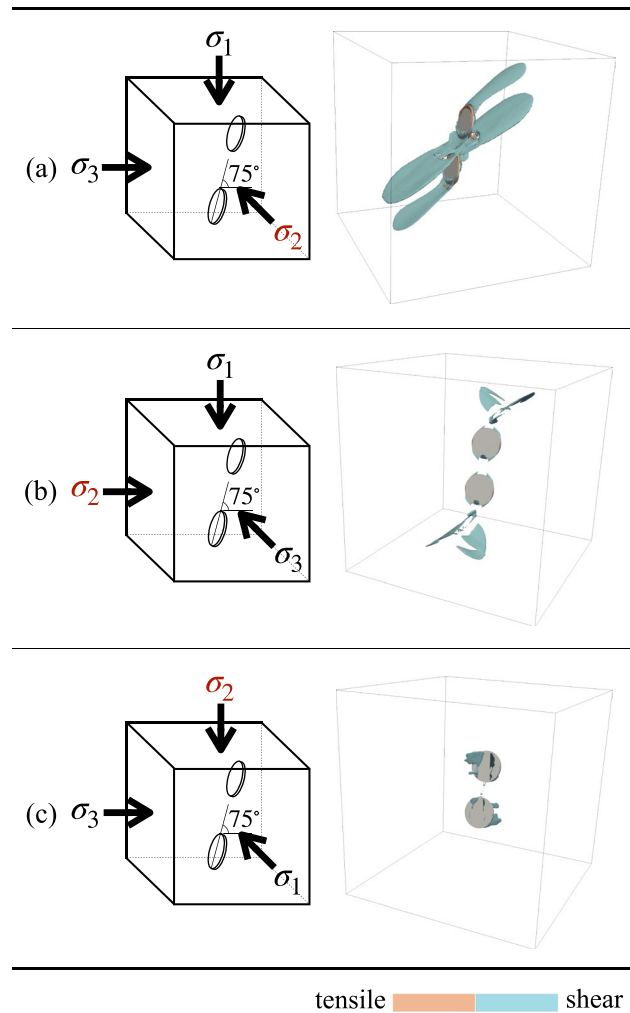


**Fig. 14** Cracking patterns in the single-flawed specimen with  $\alpha = 75^\circ$ . **a**  $\sigma_2$  is parallel to the flaw plane. **b**  $\sigma_3$  is parallel to the flaw plane. **c**  $\sigma_1$  is parallel to the flaw plane

under uniaxial and biaxial compression (Sahouryeh et al. 2002). As for the reason, recall that tensile cracks grow on the  $\sigma_1 - \sigma_2$  plane, and shear cracks grow on the  $\sigma_1 - \sigma_3$  plane. When  $\sigma_2 = \sigma_3$  (triaxial or uniaxial compression), there exist two planes for tensile/shear cracks to propagate. As such, cracks from the flaw edge tend to grow in these two planes, resulting in crack wrapping. However, when  $\sigma_2 > \sigma_3$  (true triaxial or biaxial compression), only a single plane exists for tensile/shear cracks to grow, and therefore wrapping does not occur. As the magnitude of  $\sigma_2$  becomes higher, the localized shear fracture zone becomes larger, with more or less the same cracking pattern.

In Fig. 17 we show the cracking patterns when  $\sigma_2$  is oblique to the flaw plane and  $\sigma_3$  is parallel to the flaw. It can be seen that when  $\sigma_2$  is oblique to the flaw plane, the effect of the  $\sigma_2$  magnitude becomes much more significant. In the triaxial compression regime where  $\sigma_2 = \sigma_3$



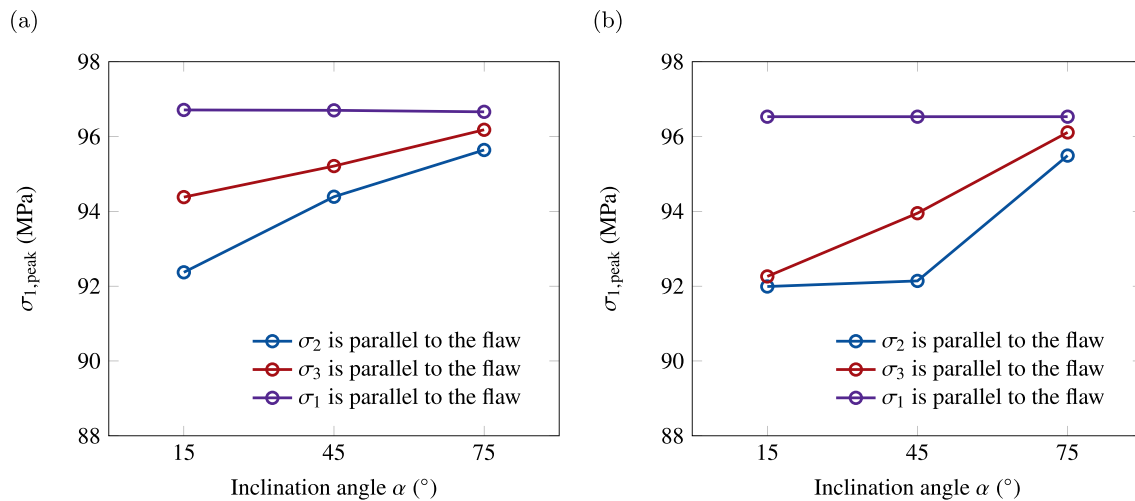


**Fig. 15** Effects of  $\sigma_2$  orientation on peak stresses. **a** Single-flawed specimens. **b** Double-flawed specimens

(Fig. 17a), branching shear cracks develop from the flaw edge (similar to the case of flaw-parallel  $\sigma_2$ , see Fig. 16a). As the magnitude of  $\sigma_2$  increases (Fig. 17b–f), however, multiple shear cracks grow in a conjugate manner, and tensile fish-fin cracks emerge. The emergence of these fish-fin cracks can be attributed to an increase in the normal stress on the flaw surface, which is  $\sigma_2$  here.

Figure 18 shows how cracking patterns are affected by the magnitude of  $\sigma_2$  when  $\sigma_1$  is parallel to the flaw. The magnitude of  $\sigma_2$  also has notable effects in this case. In the triaxial compression where  $\sigma_2 = \sigma_3$  (Fig. 18a), conjugate shear cracks propagate in the direction perpendicular to the flaw surface. As the magnitude of  $\sigma_2$  increases (Fig. 18b–e), the propagation direction of the conjugate shear cracks becomes more parallel to the orientation of  $\sigma_2$ . When  $\sigma_2$  is increased to be the same as  $\sigma_1$  (Fig. 18f), shear cracks propagate parallel to the plane of the existing flaw, like the case of flaw-parallel  $\sigma_2$  (Fig. 16f). In this orientation of principal stresses, tensile cracks are insignificant when  $\sigma_2 \leq 10$  MPa (Fig. 18a–b). However, as the magnitude of  $\sigma_2$  increases (Fig. 18c–d), it is observed that tensile cracks initiate near the flaw surface on the symmetrical plane. As the magnitude of  $\sigma_2$  approaches that of  $\sigma_1$  (Fig. 18e–f), tensile cracks grow from the upper and lower flaw tips, analogous to when  $\sigma_2$  is parallel to the flaw (Fig. 16f).

#### 4.1.2 Double Internal Flaws

Next, we examine how the magnitude of  $\sigma_2$  affects the mechanisms of crack coalescence in double-flawed specimens. Figure 19 shows the cracking patterns in double-flawed specimens subjected to different magnitudes of  $\sigma_2$ , when  $\sigma_2$  is parallel to the flaws. As in the single-flawed specimen, the

magnitude of  $\sigma_2$  has minor effect on the cracking patterns under this orientation of principal stresses. Tensile cracks initiate from the flaw tips and grow along the flaw edge and the  $\sigma_1$  orientation, and shear cracks propagate along the flaw plane. The magnitude of  $\sigma_2$  does not significantly alter the mechanism of crack coalescence.

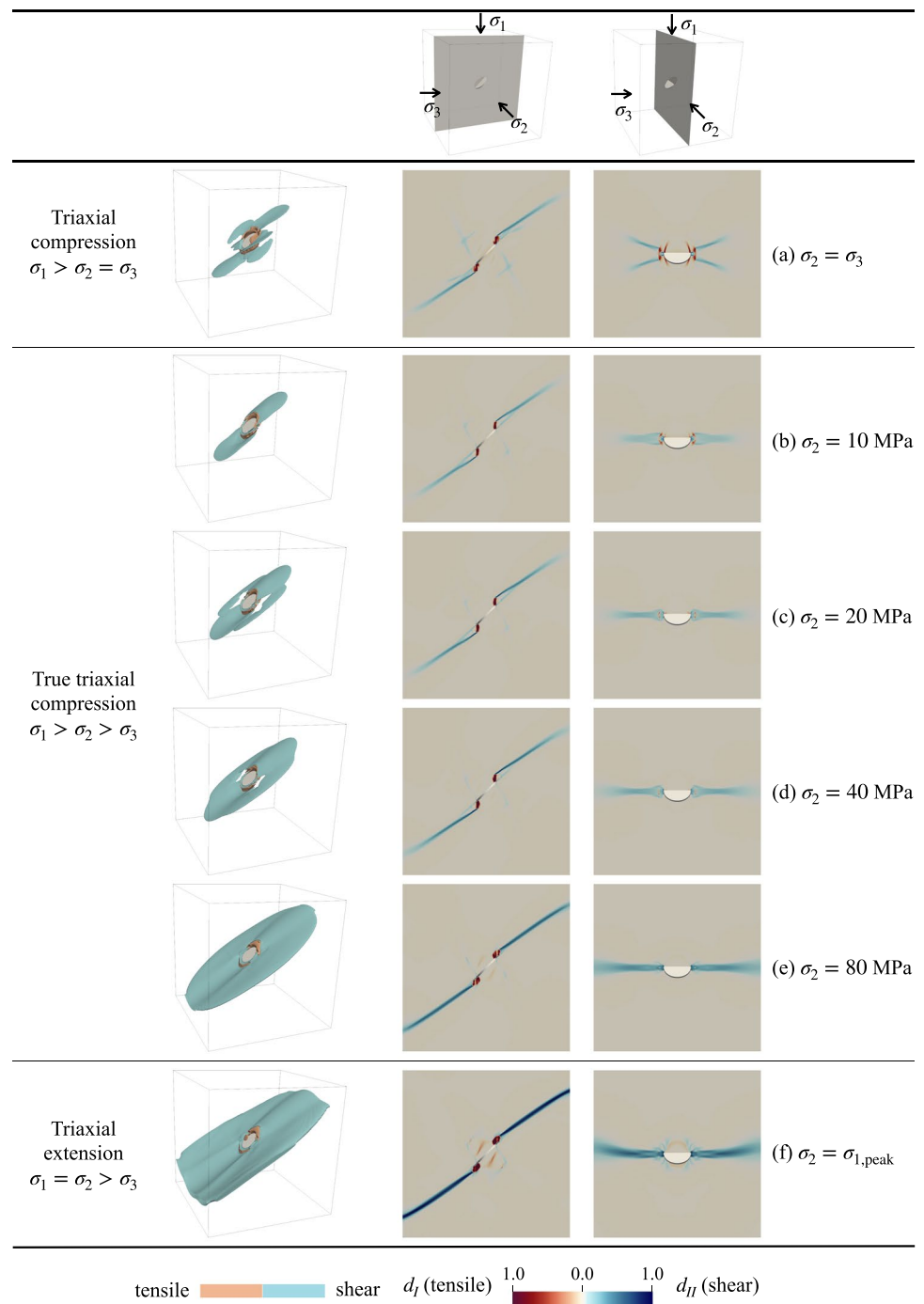
Figure 20 shows the cracking patterns when  $\sigma_3$  is parallel to the flaws. In this case, the magnitude of  $\sigma_2$  has a marked effect on the cracking patterns. As the magnitude of  $\sigma_2$  increases, conjugate shear cracks develop and tensile fish-fin cracks emerge, as in the single-flawed case (Fig. 17). As a result, the crack coalescence mechanisms in the triaxial compression regime (Fig. 20a) and other regimes (Fig. 20b–f) are quite different.

In Fig. 21 we present the effect of the  $\sigma_2$  magnitude when  $\sigma_1$  is parallel to the flaws. The overall cracking patterns and their dependence on the magnitude of  $\sigma_2$  are more or less the same as those in the single-flawed case (Fig. 18). When  $\sigma_2 \leq 40$  MPa (Fig. 21a–d), the internal flaws do not coalesce, as observed previously in Figs. 12, 13 and 14. However, when  $\sigma_2 \geq 80$  MPa (Fig. 21e–f), the internal flaws coalesce through mixed-mode cracks. This difference indicates that a high  $\sigma_2$  (close to  $\sigma_1$ ) can lead to a transition in the crack coalescence mechanism when  $\sigma_1$  is parallel to the flaws.

#### 4.2 Peak Stresses

In Fig. 22 we plot the peak stresses in the single- and double-flawed specimens compressed with different magnitudes of  $\sigma_2$ . The figure shows that the peak stresses are more or less the same in the two types of flawed specimens and that their variation with the magnitude of  $\sigma_2$  depends on what principal stress is parallel to the flaw. When  $\sigma_2$  is parallel

**Fig. 16** Cracking patterns in single-flawed specimens under different magnitudes of  $\sigma_2$ , when  $\sigma_2$  is parallel to the flaw. **a**  $\sigma_2 = \sigma_3 = 5$  MPa. **b**  $\sigma_2 = 10$  MPa. **c**  $\sigma_2 = 20$  MPa. **d**  $\sigma_2 = 40$  MPa. **e**  $\sigma_2 = 80$  MPa. **f**  $\sigma_2 = \sigma_{1,\text{peak}} = 93.53$  MPa

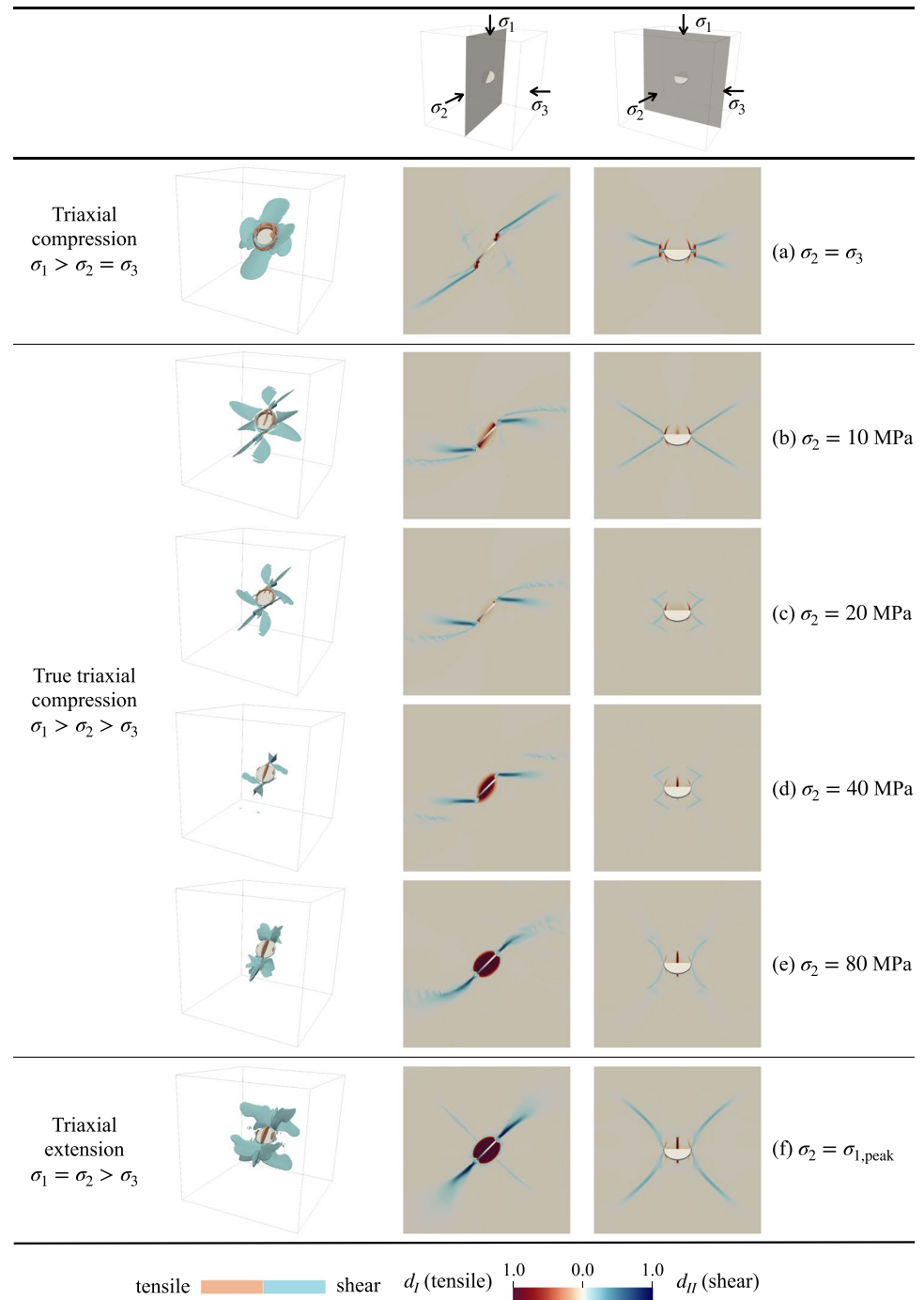


to the flaw, the magnitude of  $\sigma_2$  has little influence on the peak stress. However, when  $\sigma_3$  is parallel to the flaw, the peak stress shows a notable increase when  $\sigma_2$  increases from 5 MPa to 10 MPa (*i.e.* when the loading regime changes from triaxial compression to true triaxial compression). Conversely, when  $\sigma_1$  is parallel to the flaw, the peak stress exhibits a sharp decrease when  $\sigma_2$  increases from 80 MPa to

$\sigma_1$  (*i.e.* when the loading regime changes from true triaxial compression to triaxial extension).

In the literature, it has been agreed that the observed effects of  $\sigma_2$  on the macroscopic responses of “intact” rocks are primarily due to flaws in the rocks rather than an intrinsic property (Wiebols and Cook 1968; Haimson 2006; Kwaśniewski 2013; Browning et al. 2017). Considering this, it would be interesting to examine how

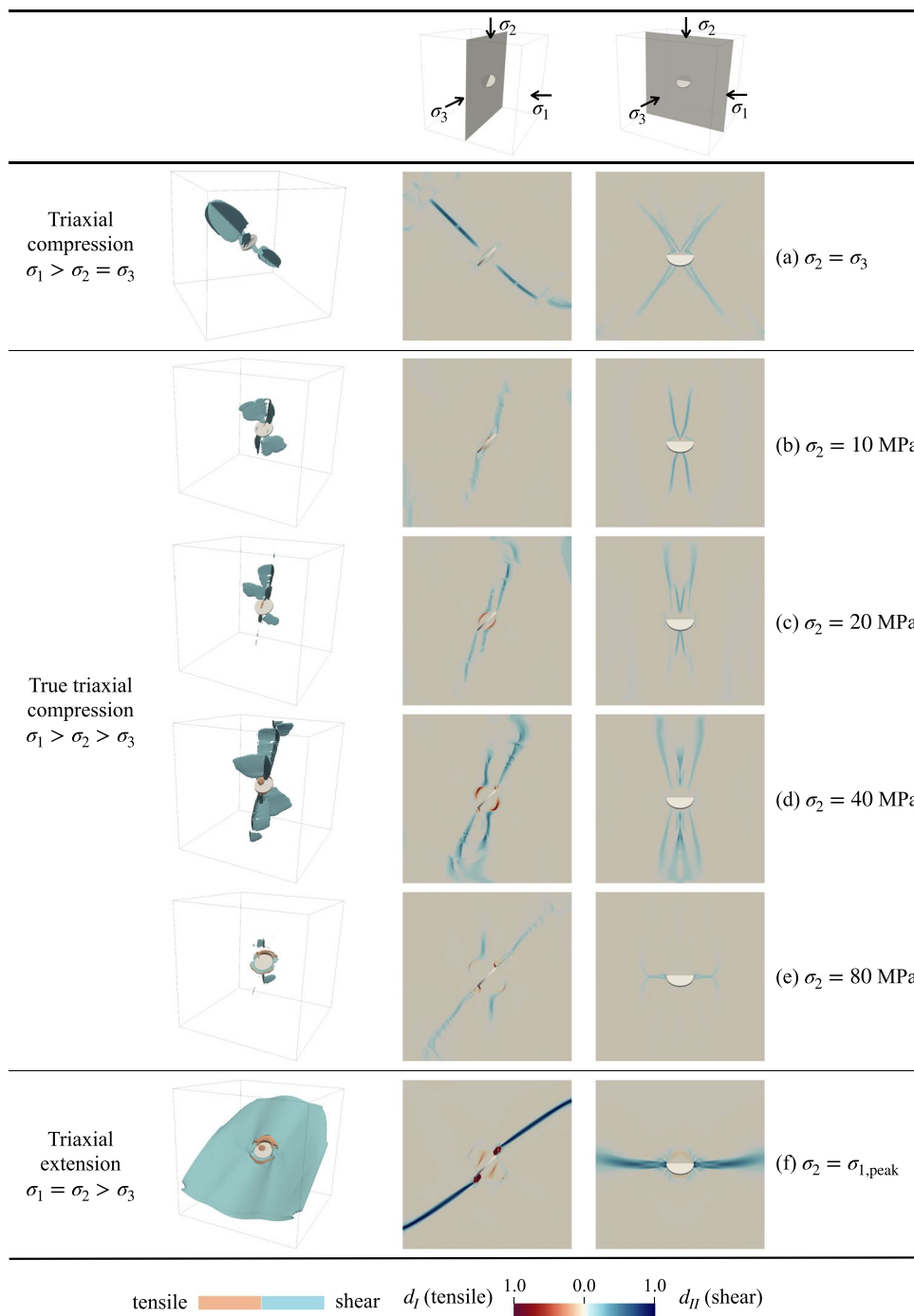
**Fig. 17** Cracking patterns in single-flawed specimens under different magnitudes of  $\sigma_2$ , when  $\sigma_3$  is parallel to the flaw. **a**  $\sigma_2 = \sigma_3 = 5$  MPa. **b**  $\sigma_2 = 10$  MPa. **c**  $\sigma_2 = 20$  MPa. **d**  $\sigma_2 = 40$  MPa. **e**  $\sigma_2 = 80$  MPa. **f**  $\sigma_2 = \sigma_{1,\text{peak}} = 95.51$  MPa



the effect of the  $\sigma_2$  magnitude manifests when the peak stresses in the three stress orientations are averaged. For this purpose, the averaged peak stresses are also drawn in Fig. 22 as dashed lines. It can be seen that the average of peak stresses exhibits an ascending-then-descending trend with an increase in  $\sigma_2$ , which is analogous to how the rock strength varies with  $\sigma_2$  in true triaxial compression (see

*e.g.* Haimson and Chang 2000; Colmenares and Zoback 2002; Ma and Haimson 2016). This observation supports the finding of Wiebols and Cook (1968) that the variation of the strength of “intact” rock specimens with  $\sigma_2$  can be attributed to cracking from randomly oriented flaws therein.

**Fig. 18** Cracking patterns in single-flawed specimens under different magnitudes of  $\sigma_2$ , when  $\sigma_1$  is parallel to the flaw. **a**  $\sigma_2 = \sigma_3 = 5$  MPa. **b**  $\sigma_2 = 10$  MPa. **c**  $\sigma_2 = 20$  MPa. **d**  $\sigma_2 = 40$  MPa. **e**  $\sigma_2 = 80$  MPa. **f**  $\sigma_2 = \sigma_{1,\text{peak}} = 93.53$  MPa



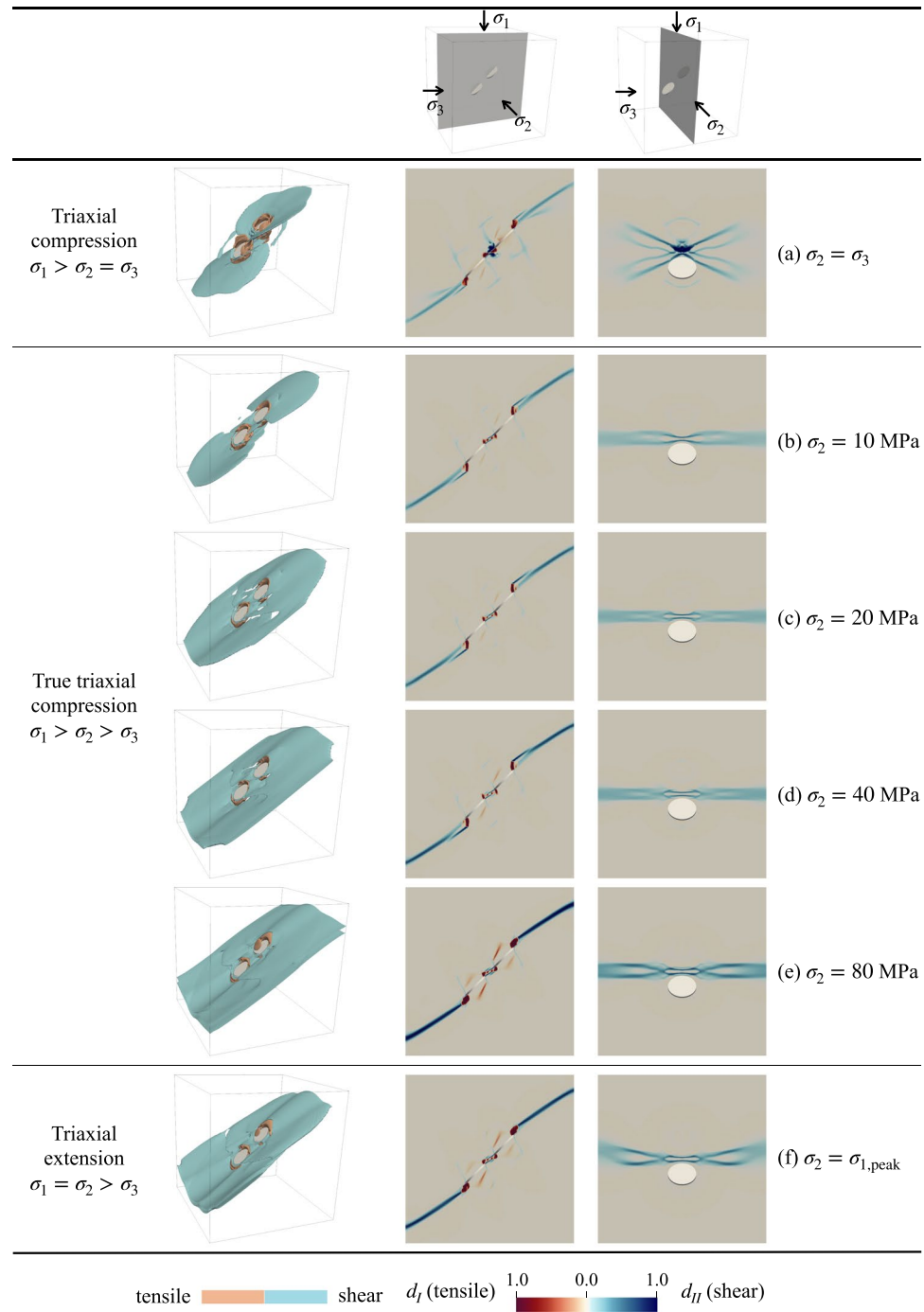
### 5 Mechanisms Underlying the Cracking Behavior Under True Triaxial Compression

In this section, we propose mechanisms underlying the cracking behavior—tensile fracture, shear fracture, and the peak stress—of 3D flawed rocks under true triaxial compression, based on the observations made in Sects. 4 and 5. For this purpose, let us consider two stresses exerted on

a 3D internal flaw—a normal stress  $\sigma_N$  and a shear stress  $\tau$  on the flaw plane—in a rock subjected to true triaxial compression, as illustrated in Fig. 23. Assuming that the flaw is closed and intact as in the work of Wiebols and Cook (1968), the specific expressions for  $\sigma_N$  and  $\tau$  can be written in terms of  $\sigma_x$  and  $\sigma_z$  as

$$\sigma_N = 0.5(\cos 2\alpha + 1)\sigma_z + 0.5(1 - \cos 2\alpha)\sigma_x, \tag{3}$$

**Fig. 19** Cracking patterns in double-flawed specimens under different magnitudes of  $\sigma_2$ , when  $\sigma_2$  is parallel to the flaw. **a**  $\sigma_2 = \sigma_3 = 5$  MPa. **b**  $\sigma_2 = 10$  MPa. **c**  $\sigma_2 = 20$  MPa. **d**  $\sigma_2 = 40$  MPa. **e**  $\sigma_2 = 80$  MPa. **f**  $\sigma_2 = \sigma_{1,peak} = 91.11$  MPa



$$\tau = 0.5 \sin 2\alpha(\sigma_z - \sigma_x). \tag{4}$$

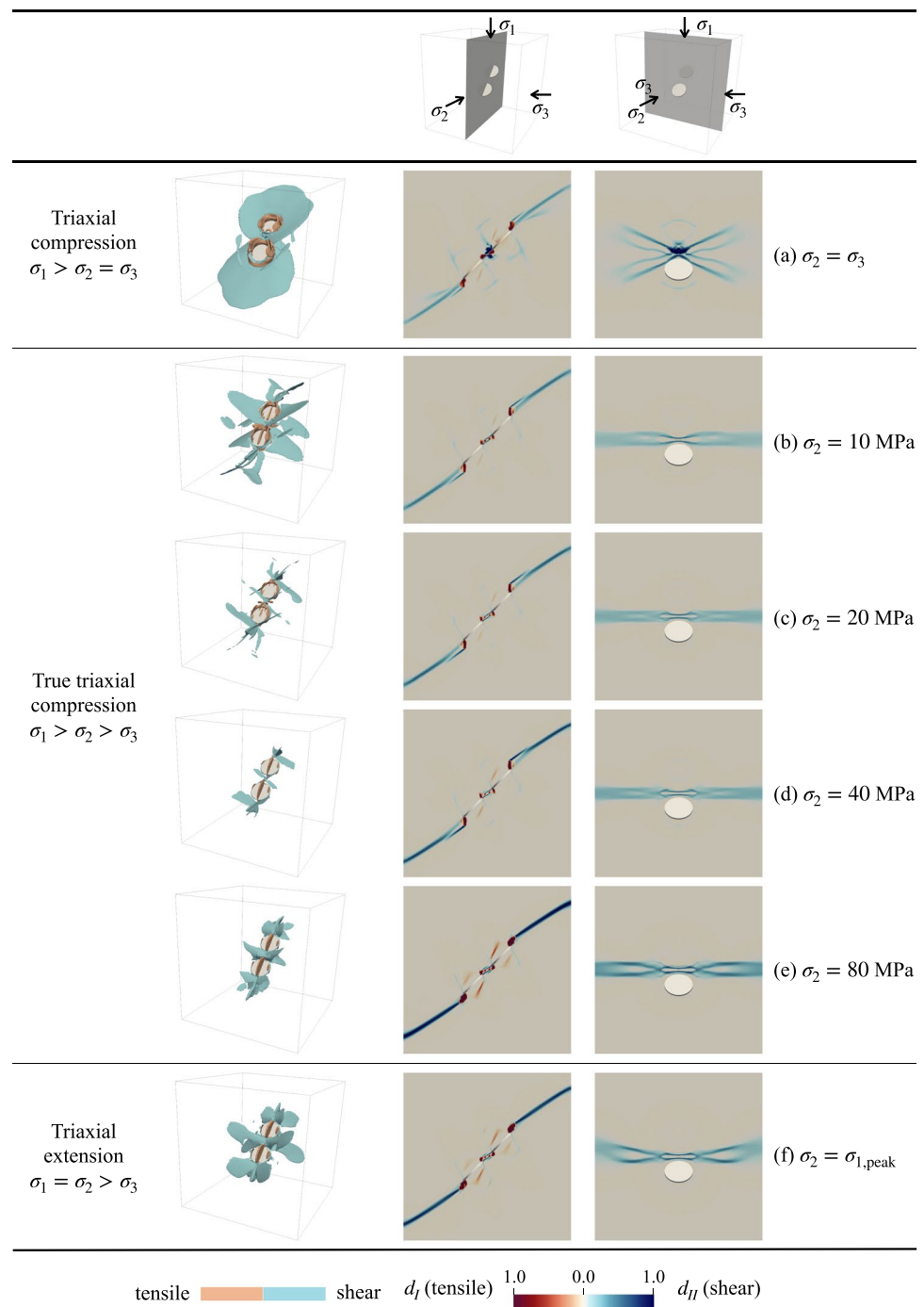
In the following, we discuss how the individual or combined effect of  $\sigma_N$  and  $\tau$  can explain the cracking patterns and peak stresses characterized in this study.

### 5.1 Mechanism of Tensile Fracture: Control of the Normal Stress on the Flaw

First, we propose that a higher  $\sigma_N$  promotes the propagation of tensile cracks from the flaw. This is because a higher  $\sigma_N$  tends to expand the flaw in the radial direction, giving rise to higher tensile hoop stresses along the flaw edge. Consequently, the tensile crack can initiate earlier on the flaw and have more propagation. This mechanism explains why tensile fractures appear in Fig. 9a–b, whereas they are absent



**Fig. 20** Cracking patterns in double-flawed specimens under different magnitudes of  $\sigma_2$ , when  $\sigma_3$  is parallel to the flaw. **a**  $\sigma_2 = \sigma_3 = 5$  MPa. **(b)**  $\sigma_2 = 10$  MPa. **c**  $\sigma_2 = 20$  MPa. **d**  $\sigma_2 = 40$  MPa. **e**  $\sigma_2 = 80$  MPa. **f**  $\sigma_2 = \sigma_{1,\text{peak}} = 94.62$  MPa

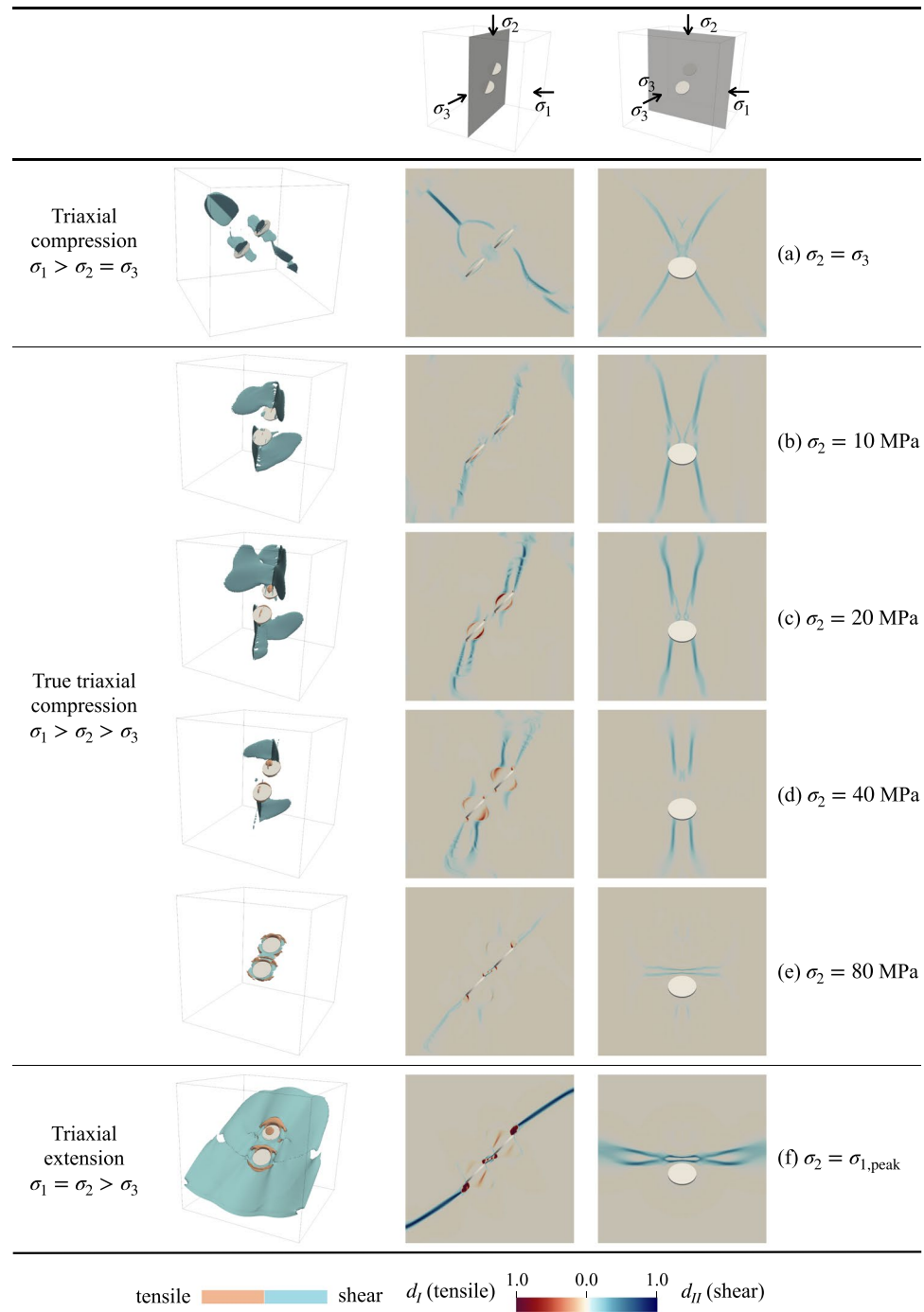


in Fig. 9c in which  $\sigma_z = \sigma_2$  gives a lower  $\sigma_N$  than the first two cases with  $\sigma_z = \sigma_1$  according to Eq. (3). The same trend can also be observed in other cases with different inclination angles, see, e.g. Figs. 10 and 11. Therefore, the mechanism proposed here is consistent with observations made in Sect. 4.

## 5.2 Mechanism of Shear Fracture: Control of the Coulomb Stress on the Flaw

Second, we propose that shear cracks tend to propagate more along the flaw plane that has a higher Coulomb stress. The Coulomb stress can be written as Cocco and Rice (2002)

**Fig. 21** Cracking patterns in double-flawed specimens under different magnitudes of  $\sigma_2$ , when  $\sigma_1$  is parallel to the flaw. **a**  $\sigma_2 = \sigma_3 = 5$  MPa. **b**  $\sigma_2 = 10$  MPa. **c**  $\sigma_2 = 20$  MPa. **d**  $\sigma_2 = 40$  MPa. **e**  $\sigma_2 = 80$  MPa. **f**  $\sigma_2 = \sigma_{1,peak} = 91.11$  MPa



$$\begin{aligned} \sigma_{\text{Coulomb}} &= \tau - \mu\sigma_N \\ &= 0.5(\sin 2\alpha - \mu \cos 2\alpha - \mu)\sigma_z \\ &\quad + 0.5(\mu \cos 2\alpha - \mu - \sin 2\alpha)\sigma_x. \end{aligned} \tag{5}$$

It can be seen that the Coulomb stress represents the excess of the shear stress beyond the frictional strength. Therefore, a higher Coulomb stress on the flaw plane leads to more sliding (Mode II motion) and hence a higher tendency to generate shear cracks along the flaw plane. This mechanism

can be corroborated by the different shear crack patterns observed in Fig. 9a–c. Specifically, one can observe shear fracture propagation along the flaw plane when  $\sigma_y = \sigma_2$  (Fig. 9a) which gives the highest Coulomb stress according to Eq. (5). By contrast, Fig. 9b–c show that shear cracks deviate significantly from the flaw plane, as the maximum Coulomb stress does not align with the flaw plane in these two cases.

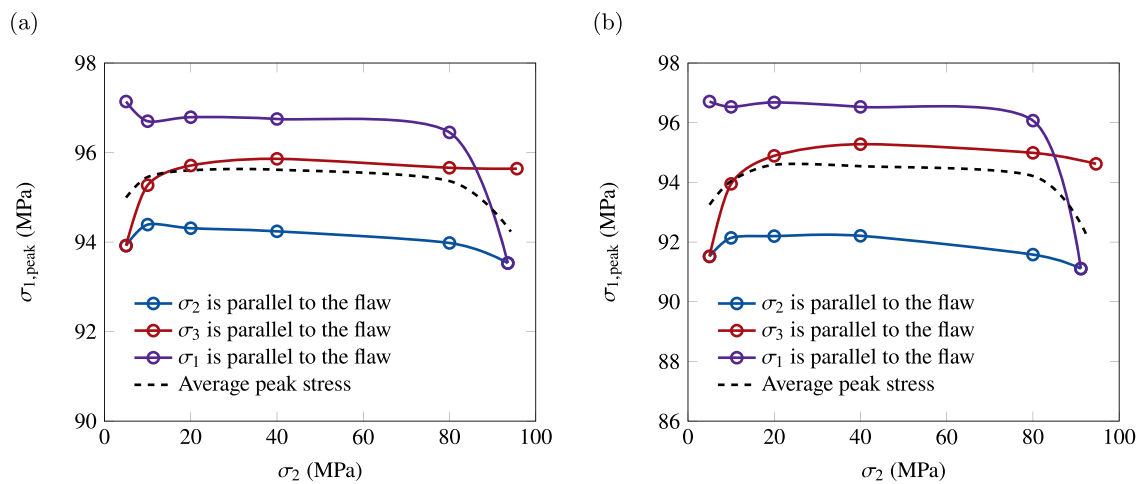
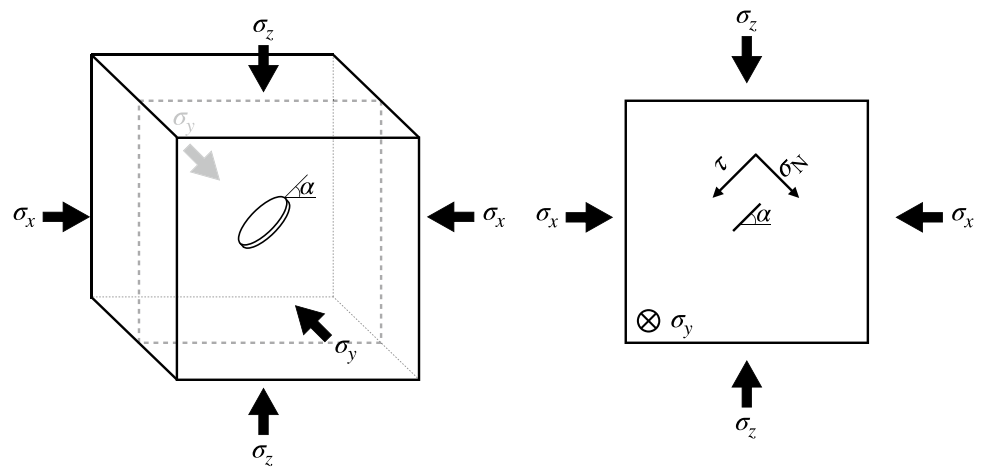


**Fig. 22** Effects of  $\sigma_2$  magnitude on the peak stress. **a** Single-flawed specimens; **b** Double-flawed specimens

**Fig. 23** Stress state around a 3D internal flaw subjected to true triaxial compression



### 5.3 Mechanism of Peak Stress: Control of the Mixed-Mode Cracking Pattern

Third, we propose that there is a correlation between the peak stress and the mixed-mode cracking pattern. It is known that the failure of the specimen is mainly triggered by the development of critical shear cracks around the flaw, especially those along the flaw plane (Wong 2008). Therefore, it can be postulated that the peak stress is lower when the shear crack plane overlaps the flaw plane more (*i.e.* shear cracks more parallel with the flaw), as the open flaw has no strength and thus provides little resistance to shear loading. This can be evidenced by the effects of  $\sigma_2$  orientation in Fig. 15: When  $\sigma_2$  is parallel to the flaw, *i.e.* potential shear cracks more aligned with the flaw plane, the peak stress is consistently the lowest. As for the effects of the tensile fracture, we can conjecture that the peak stress may be higher when more tensile cracks are generated from the flaw. This is because tensile fractures from the flaw commonly grow

in a stable manner (Bobet and Einstein 1998b; Wong and Einstein 2009d), thus they do not have detrimental effects on material stiffness and strength. See Figs. 6 and 7 where the slopes of the pre-peak stress–strain curves show marginal changes despite the significant development of tensile cracks. Additionally, tensile crack propagation could release the stress around the flaw; it thus impedes the growth of more shear cracks and eventually delays the failure of the specimen.

Combining the mechanisms of tensile and shear fractures discussed earlier, we propose the Coulomb-to-normal stress ratio as a quantitative measure of the effects of the mixed-mode cracking pattern on the peak stress, as

$$\frac{\sigma_{\text{Coulomb}}}{\sigma_{\text{N}}} = \frac{\sin 2\alpha}{\cos 2\alpha + (\sigma_z + \sigma_x)/(\sigma_z - \sigma_x)} - \mu. \quad (6)$$

Based on the postulated relationship between the peak stress and the mixed-mode cracking pattern, we suggest that the

peak stress is higher when this stress ratio is lower. Also notably, because this Coulomb-to-normal stress ratio is a function of the principal stresses (*i.e.*  $\sigma_x$  and  $\sigma_y$ ), it can help explain the effects of the orientation and magnitude of  $\sigma_2$  on the peak stress. Specifically, the peak stress variations observed in this study can be explained as follows.

- In Fig. 15, the peak stress shows a large variation with the flaw inclination angle when  $\sigma_2$  or  $\sigma_3$  is parallel to the flaw (*i.e.*  $\sigma_y = \sigma_2$  or  $\sigma_3$ ), whereas it remains nearly constant when  $\sigma_1$  is parallel to the flaw (*i.e.*  $\sigma_y = \sigma_1$ ). This is because when  $\sigma_y = \sigma_2$  or  $\sigma_3$ , the value of  $(\sigma_z + \sigma_x)/(\sigma_z - \sigma_x)$  is almost equal to 1 since  $\sigma_z$  ( $= \sigma_1 > 90$  MPa) is much larger than  $\sigma_2$  (10 MPa) and  $\sigma_3$  (5 MPa). As a result, the stress ratio defined in Eq. (6) is more sensitive to the flaw inclination angle and so leads to a larger difference in the peak stress. By contrast, when  $\sigma_y = \sigma_1$ , the value of  $(\sigma_z + \sigma_x)/(\sigma_z - \sigma_x)$  in the denominator of Eq. (6) becomes greater, *i.e.*  $(\sigma_z + \sigma_x)/(\sigma_z - \sigma_x) = (\sigma_2 + \sigma_3)/(\sigma_2 - \sigma_3) = 3$ . In this case, the stress ratio is less sensitive to  $\alpha$  and thus results in smaller changes in the peak stress.
- Figure 22 shows how the peak stress varies with the magnitude of  $\sigma_2$  under three cases of principal stress orientations. As discussed in Sect. 5, when  $\sigma_2$  is parallel to the flaw, the peak stress manifests little variation with the magnitude of  $\sigma_2$ . This can be explained by that the Coulomb-to-normal stress ratio remains unchanged in this case. When  $\sigma_3$  is parallel to the flaw, the peak stress increases with the  $\sigma_2$  magnitude. This can be explained that as  $\sigma_x = \sigma_2$  increases, the stress ratio decreases (the denominator increases) and makes the peak stress higher. Conversely, when  $\sigma_1$  is parallel to the flaw, the peak stress decreases with the magnitude of  $\sigma_2$ . This can be explained by that as  $\sigma_z = \sigma_2$  increases, the stress ratio increases (the denominator decreases), and the peak stress becomes reduced.

As explained above, the proposed Coulomb-to-normal stress ratio is not only a reasonable indicator for the control of mixed-mode cracking pattern on the peak stress of a flawed specimen under true triaxial compression, but it also provides insight into the effects of the orientation and magnitude of  $\sigma_2$  on the peak stress.

## 6 Conclusions

This study has performed a numerical investigation into the effects of the intermediate principal stress ( $\sigma_2$ ) on the 3D cracking process in flawed rocks under true triaxial compression. Through the use of a fracture-mechanics-based and well-validated simulation method for mixed-mode fracture,

we have investigated how the orientation and magnitude of  $\sigma_2$  affect the cracking patterns and peak stress. Based on the results of the investigation, the following conclusions can be drawn:

1. The orientation of  $\sigma_2$  has significant effects on the cracking pattern of flawed rocks under true triaxial compression. Tensile cracks propagate on the  $\sigma_1 - \sigma_2$  plane, and shear cracks propagate along the path that lies on the  $\sigma_1 - \sigma_3$  plane.
2. In most cases, the orientation of principal stresses has a greater effect on the cracking pattern than the flaw inclination angle.
3. The orientation of  $\sigma_2$  also controls the peak stress in flawed rocks under compression. The peak stress is highest when  $\sigma_1$  is parallel to the flaw, whereas it is lowest when  $\sigma_2$  is parallel to the flaw.
4. The magnitude of  $\sigma_2$  affects the cracking pattern and peak stress differently depending on the orientation of principal stresses. The effect of the  $\sigma_2$  magnitude is significant when  $\sigma_2$  is oblique to the flaw plane, whereas it is marginal when  $\sigma_2$  is parallel to the flaw.
5. Three mechanisms are proposed to explain the observed  $\sigma_2$  effects on the cracking behavior of 3D flawed rocks under true triaxial compression. They are: (i) the tensile fracture is controlled by the normal stress on the flaw; (ii) the shear fracture is controlled by the Coulomb stress on the flaw; and (iii) the peak stress is controlled by the mixed-mode cracking pattern which can be explained by the Coulomb-to-normal stress ratio.

## Appendix 1: Double-phase-field formulation for 3D mixed-mode fracture in rocks

This appendix provides detailed explanations of the formulation of the double-phase-field model.

### Appendix 1.1: Governing Equations

The governing equations of the double-phase-field model are derived from microforce theory for phase-field modeling of fracture (da Silva Jr et al. 2013). The two microforce balance equations for tensile and shear fractures are given by

$$\nabla \cdot \left( \frac{\partial \psi(\epsilon, d_I, \nabla d_I, d_{II}, \nabla d_{II})}{\partial \nabla d_I} \right) - \frac{\partial \psi(\epsilon, d_I, \nabla d_I, d_{II}, \nabla d_{II})}{\partial d_I} = 0 \quad (\text{Microforce balance for tensile fracture}), \quad (7)$$

$$\begin{aligned} \nabla \cdot \left( \frac{\partial \psi(\epsilon, d_I, \nabla d_I, d_{II}, \nabla d_{II})}{\partial \nabla d_{II}} \right) - \frac{\partial \psi(\epsilon, d_I, \nabla d_I, d_{II}, \nabla d_{II})}{\partial d_{II}} \\ = 0 \text{ (Microforce balance for shear fracture),} \end{aligned} \tag{8}$$

where  $\psi(\epsilon, d_I, \nabla d_I, d_{II}, \nabla d_{II})$  is the potential energy density and  $\epsilon$  is the (infinitesimal) strain tensor.

The potential energy density in Eqs. (7) and (8) is decomposed into three parts as

$$\psi = \psi^e + \psi^f + \psi^d, \tag{9}$$

where  $\psi^e$  is the elastic strain energy,  $\psi^f$  is the energy dissipation due to frictional sliding along a crack, and  $\psi^d$  is the energy dissipation due to the generation of a new crack surface. The external energy due to body forces is ignored here. The specific expressions of these energy densities are presented below. (For brevity, their mathematical derivations are omitted and referred to Fei and Choo 2021.)

*Strain energy* Due to the incremental nonlinearity of the phase-field model for frictional shear fracture (Fei and Choo 2020a, b), the strain energy density is formulated in its rate form, as

$$\dot{\psi}^e = [g_I(d_I)\bar{\sigma}_I^+ + g_{II}(d_{II})\bar{\sigma}_{II}^+ + \bar{\sigma}^-] : \dot{\epsilon}. \tag{10}$$

Here,  $\bar{\sigma}_I^+$  and  $\bar{\sigma}_{II}^+$  denote the tensile and shear parts of the undamaged stress tensor  $\bar{\sigma}$ , respectively. The remaining stress term  $\bar{\sigma}^- := \bar{\sigma} - \bar{\sigma}_I^+ - \bar{\sigma}_{II}^+$  is the pure compression part which does not contribute to fracturing. Detailed expressions for these stress components can be obtained considering the direction and contact condition of the crack, see Fei and Choo (2021).

*Frictional dissipation* The rate of the frictional dissipation is calculated according to the crack’s contact condition as

$$\dot{\psi}^f = \begin{cases} 0 & \text{if open,} \\ 0 & \text{if stick,} \\ [1 - g_{II}(d_{II})] \tau_r \dot{\gamma} & \text{if slip,} \end{cases} \tag{11}$$

where  $\tau_r$  is the residual frictional strength of the crack, and  $\gamma$  is the total shear strain in the slip direction.

*Fracture dissipation* The fracture energy dissipation is the sum of the energy dissipation associated with the creation of tensile crack surface,  $\psi_I^d$ , and that associated with the creation of shear crack surface,  $\psi_{II}^d$ , as

$$\psi^d = \psi_I^d + \psi_{II}^d. \tag{12}$$

The two fracture dissipation terms can be expressed as

$$\psi_I^d = \mathcal{G}_I \Gamma_{d_I} = \frac{\mathcal{G}_I}{\pi L} [(2d_I - d_I^2) + L^2(\nabla d_I)^2], \tag{13}$$

$$\psi_{II}^d = \mathcal{G}_{II} \Gamma_{d_{II}} = \frac{\mathcal{G}_{II}}{\pi L} [(2d_{II} - d_{II}^2) + L^2(\nabla d_{II})^2], \tag{14}$$

where  $\Gamma_{d_I}$  and  $\Gamma_{d_{II}}$  are the crack density functions used for phase-field regularization of tensile and shear fractures, respectively. For both of them, we adopt the specific form proposed by Wu (2017) for cohesive phase-field fracture.

Inserting the above energy densities into Eqs. (7) and (8), we arrive at the following form of the governing equations

$$-g'_I(d_I)\mathcal{H}_I - \frac{\mathcal{G}_I}{\pi L} (2L^2 \nabla \cdot \nabla d_I - 2 + 2d_I) = 0, \tag{15}$$

$$-g'_{II}(d_{II})\mathcal{H}_{II} - \frac{\mathcal{G}_{II}}{\pi L} (2L^2 \nabla \cdot \nabla d_{II} - 2 + 2d_{II}) = 0, \tag{16}$$

which are the same as Eqs. (1) and (2). Here,  $\mathcal{H}_I$  and  $\mathcal{H}_{II}$  are crack driving forces for tensile and shear fractures, respectively. In the following, we describe crack driving forces suitable for mixed-mode fracture in quasi-brittle rocks.

### Appendix 1.2: Crack Driving Forces for Mixed-Mode Fracture in Quasi-Brittle Rocks

The crack driving forces of the double-phase-field model are derived from the  $\mathcal{F}$ -criterion proposed by Shen and Stephansson (1994) for mixed-mode fracture in rock. In essence, the  $\mathcal{F}$ -criterion asserts that mixed-mode fracture takes place such that it maximizes the energy dissipation. In the context of the double-phase-field formulation, it can be represented as

$$\theta = \arg \max_{\theta} [\mathcal{F}(\theta)]_{\epsilon}, \quad \text{with } \mathcal{F}(\theta) := \frac{\mathcal{H}_I(\epsilon, \theta)}{\mathcal{G}_I} + \frac{\mathcal{H}_{II}(\epsilon, \theta)}{\mathcal{G}_{II}}. \tag{17}$$

Here,  $\theta$  is defined as the angle between the crack normal direction and the major principal stress direction on the slip plane, and it enters the calculation of elastic strain energy  $\psi^e$  and frictional dissipation  $\psi^f$ .

Based on the  $\mathcal{F}$ -criterion and the governing equations, the tensile and shear crack driving forces are formulated according to the damage state and the contact condition. Specific expressions for the four possible cases are presented below.

*Intact (undamaged) condition* In quasi-brittle materials, damage is assumed to develop only when the stress reaches tensile or shear strength. To impose this behavior, we set  $\mathcal{H}_I$  and  $\mathcal{H}_{II}$  as their thresholds calculated by the tensile and shear strengths, namely



$$\left. \begin{aligned} \mathcal{H}_I &= \mathcal{H}_{I,t} = \frac{1}{2M} \sigma_p^2 \\ \mathcal{H}_{II} &= \mathcal{H}_{II,t} = \frac{1}{2G} (\tau_p - \tau_r)^2 \end{aligned} \right\} \text{if intact,} \tag{18}$$

where  $M := K + (4/3)G$  is the 1D constrained modulus, with  $K$  and  $G$  denoting the bulk and shear moduli, respectively. Also,  $\sigma_p$  is a constant tensile strength, and  $\tau_p$  and  $\tau_r$  are the peak and residual shear strengths, respectively. Adopting the Mohr-Coulomb criterion, the peak and residual strengths are expressed as

$$\tau_p = c_0 + p_N \tan \phi, \tag{19}$$

$$\tau_r = p_N \tan \phi, \tag{20}$$

where  $p_N$  is the normal pressure,  $c_0$  is the cohesion, and  $\phi$  is the frictional angle. By setting these crack driving forces to their thresholds and employing degradation functions of particular form (explained in the next section), Eqs. (15) and (16) enforce zero damages (*i.e.*  $d_I = 0$  and  $d_{II} = 0$ ) before the stress reaches strength.

*Open condition* When the crack is open, maximizing  $\mathcal{F}$  leads to  $\theta = 0$ , see Fei and Choo (2021) for detailed derivation. This suggests that if the potential contact state is an open condition, the crack should grow in its normal direction aligned with the major principal stress direction. In this case, we have

$$\left. \begin{aligned} \mathcal{H}_I &= \frac{1}{2M} \bar{\sigma}_1^2 \\ \mathcal{H}_{II} &= 0 \end{aligned} \right\} \text{if open,} \tag{21}$$

where  $\bar{\sigma}_1$  is the major principal stress. Note that in this case, the shear crack driving force is zero because shear stress is absent on the principal stress plane.

*Stick condition* When the crack is closed and stick, we have  $\bar{\sigma}_1^+ = \bar{\sigma}_{II}^+ = 0$  because both compressive and shear stresses can be transferred across the crack surface without degrading any stress components. Thus, in this case  $\partial \psi^e / \partial d_I = \partial \psi^e / \partial d_{II} = 0$ . Also, there is no frictional dissipation, *i.e.*  $\psi^f = 0$ . Therefore, we obtain

$$\left. \begin{aligned} \mathcal{H}_I &= 0 \\ \mathcal{H}_{II} &= 0 \end{aligned} \right\} \text{if stick.} \tag{22}$$

*Slip condition* When the crack is closed and undergoing slip,  $\mathcal{H}_I = 0$  because tensile stress is zero (*i.e.*  $\bar{\sigma}_1^+ = 0$ ). As a result, maximizing  $\mathcal{F}$  in this case is equivalent to maximizing  $\mathcal{H}_{II}$ . According to the phase-field formulation for frictional shear fracture (Fei and Choo 2020b), the maximization task eventually becomes

$$\theta = \arg \max_{\theta} [\bar{\tau}(\theta) - \tau_r(\theta)], \tag{23}$$

where  $\bar{\tau}$  is the shear component of the undamaged stress  $\bar{\sigma}$  in the crack direction, and  $\tau_r$  is the residual shear strength introduced in Eq. (20). Under a plane strain condition, it is straightforward to get

$$\theta = 45^\circ - \frac{\phi}{2}. \tag{24}$$

Under a 3D condition, the problem becomes a bit more complicated because there is an infinite number of planes that satisfy the condition described above. Therefore, for 3D problems, we introduce another condition that the potential crack path lies on the  $\sigma_1 - \sigma_3$  plane, because this plane provides the maximum deviatoric stress as can be easily seen in the Mohr Circle. Having specified the direction of shear fracture, we can evaluate the undamaged shear stress and the shear strain in the crack slip direction,  $\bar{\tau}$  and  $\gamma$ , respectively. Eventually, we obtain

$$\left. \begin{aligned} \mathcal{H}_I &= 0 \\ [0.5em] \mathcal{H}_{II} &= \mathcal{H}_{II,t} + \mathcal{H}_{\text{slip}} \end{aligned} \right\} \text{if slip, with } \mathcal{H}_{\text{slip}} := \int_{\gamma_p}^{\gamma} (\bar{\tau} - \tau_r) d\gamma. \tag{25}$$

Here,  $\mathcal{H}_{\text{slip}}$  represents the crack driving force accumulated during the post-peak slip process, and  $\gamma_p$  is the shear strain in the slip direction when  $\tau = \tau_p$ . Expanding  $\mathcal{H}_{\text{slip}}$  gives

$$\mathcal{H}_{\text{slip}} := \underbrace{\int_{\gamma_p}^{\gamma} \bar{\tau} d\gamma}_{\text{release of stored energy}} - \underbrace{\int_{\gamma_p}^{\gamma} \tau_r d\gamma}_{\text{frictional dissipation}}. \tag{26}$$

As discussed in Fei and Choo (2020b), the above equation is consistent with the fracture mechanics theory proposed by Palmer and Rice (1973) for frictional shear discontinuities in geologic materials. In a nutshell, the theory describes the growth of a shear crack in terms of the balance between the release of stored energy and the sum of fracture dissipation and frictional dissipation. One can see that Eq. (26) is consistent with the fracture mechanics theory of Palmer and Rice.

### Appendix 1.3: Degradation Functions Ensuring Length Insensitivity

To complete the double-phase-field formulation, it is necessary to specify the degradation functions for tensile and shear fractures,  $g_I(d_I)$  and  $g_{II}(d_{II})$ , respectively. The standard phase-field formulation for brittle fracture uses a quadratic degradation function in the form of  $g(d) = (1 - d)^2$ , see *e.g.* (Choo and Sun 2018b; Ha et al. 2018; Santillán et al. 2018). It is well known that when this quadratic

degradation function is used, the strength (peak stress) of the material must be controlled by the phase-field regularization length,  $L$ . For quasi-brittle materials, however, the strength should be independent of the phase-field regularization length, because it is a designated material parameter. Therefore, recent phase-field models of quasi-brittle fracture (e.g. Wu 2017; Geelen et al. 2019; Fei and Choo 2020b) employ non-standard degradation functions that are derived to make the strength insensitive to the phase-field regularization length.

The degradation functions of the double-phase-field formulation adopt the common form of  $g(d)$  for quasi-brittle fracture, given by

$$g(d) = \frac{(1-d)^n}{(1-d)^n + md(1+pd)}. \quad (27)$$

For both tensile and shear degradation functions, we use  $n = 2$  and  $p = -0.5$  to be compatible with the crack density

functions in Eqs. (13) and (14). The expression for  $m$  is determined by ensuring  $d = 0$  at the intact state when the crack driving forces are equal to their threshold values. Through this procedure, we get

$$g_I(d_I) = \frac{(1-d_I)^2}{(1-d_I)^2 + m_I d_I (1-0.5d_I)}, \quad (28)$$

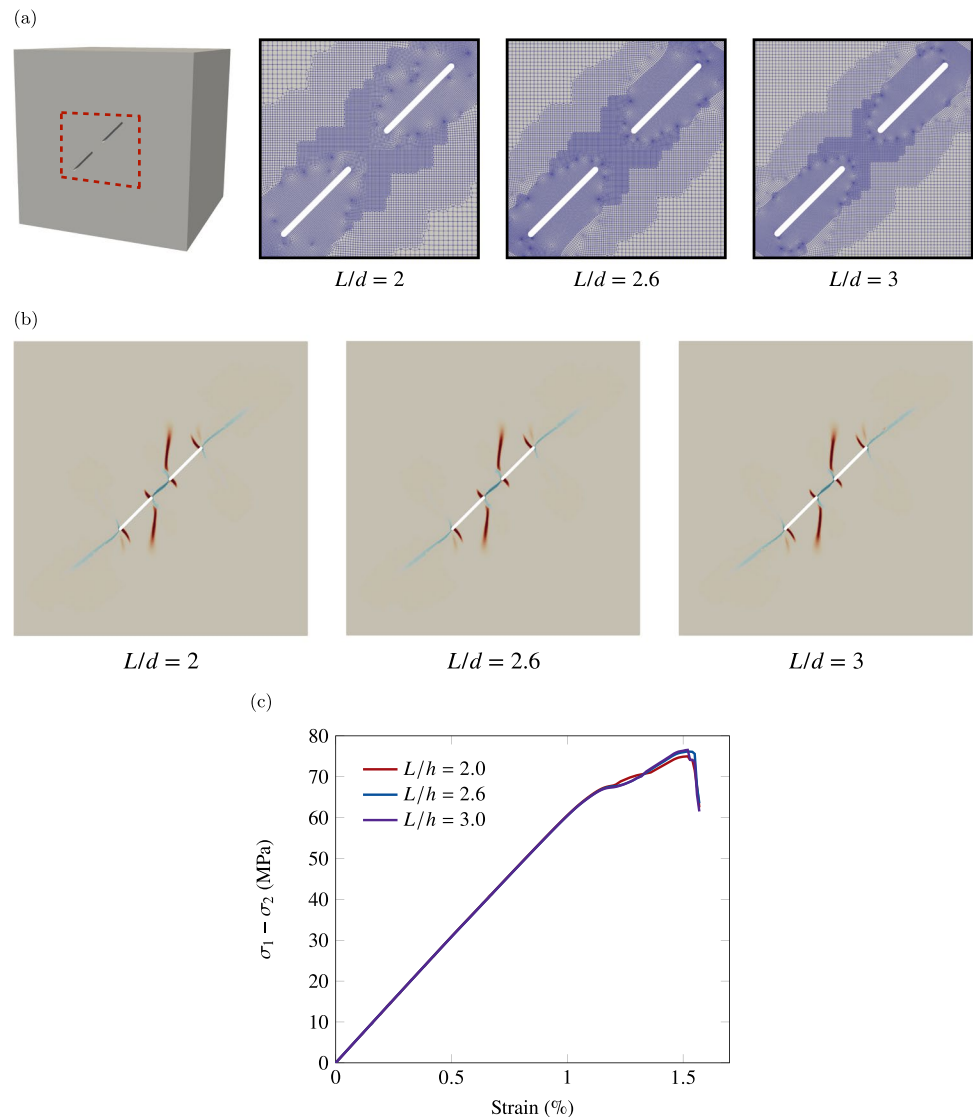
with  $m_I := \frac{G_I}{\pi L \mathcal{H}_{I,t}}$ ,

and

$$g_{II}(d_{II}) = \frac{(1-d_{II})^2}{(1-d_{II})^2 + m_{II} d_{II} (1-0.5d_{II})}, \quad (29)$$

with  $m_{II} := \frac{G_{II}}{\pi L \mathcal{H}_{II,t}}$ .

**Fig. 24** Mesh sensitivity analysis of the problem of cracking from two coplanar 2D flaws under true triaxial compression. **a** Meshes used. **b** Cracking patterns at the peak stress. **c** Stress–strain curves



Analysis of the above degradation functions in a 1D setting shows that the tensile and shear stress of the phase-field model are insensitive to the phase-field regularization length. Specifically, according to the analysis of Geelen et al. (2019) for tensile crack, the 1D tensile stress during the evolution of cohesive tensile fracture is given by

$$\sigma(d_I^*) = \sqrt{\frac{d_I^*(1-d_I^*)^2}{d_I^*(1-0.5d_I^*)}} \sigma_p^2. \quad (30)$$

Likewise, the 1D shear stress during the evolution of frictional shear fracture is given by Fei and Choo (2020b)

$$\tau(d_{II}^*) = \sqrt{\frac{d_{II}^*(1-d_{II}^*)^2}{d_{II}^*(1-0.5d_{II}^*)}} (\tau_p - \tau_r)^2. \quad (31)$$

Here,  $d_I^*$  and  $d_{II}^*$  represent the maximum damage values at the diffuse interfaces for tensile and shear cracks, respectively. It can be seen that neither Eqs. (30) nor (31) is a function of the phase-field regularization length,  $L$ .

## Appendix 2: Mesh Sensitivity Study

In this appendix, we examine the mesh sensitivity of the double-phase-field method for simulating cracking from 3D flaws under true triaxial compression. For this purpose, we repeat the validation example in Sect. 3.2.1 with three different meshes depicted in Fig. 24a. The three meshes are created with different levels of local refinement, namely  $L/h = 2, 2.6, \text{ and } 3$ , fixing the phase-field regularization length as  $L = 0.3 \text{ mm}$ . Figure 24 compares the simulation results obtained with the three different meshes. One can see from Fig. 24b that the cracking patterns obtained with the three meshes are virtually identical. Also, as shown in Fig. 24c, the stress–strain curves exhibit very little sensitivity to the element size. Thus it can be concluded that the simulation results are insensitive to the mesh as long as  $L/h \geq 2$ .

**Acknowledgements** The authors are grateful to Professor John W. Rudnicki and the other two anonymous reviewers for their constructive reviews.

**Funding** Open Access funding enabled and organized by KAIST. This work was supported by the Research Grants Council of Hong Kong (Project No. 17201419) and the National Research Foundation of Korea (NRF) grant funded by the Korean government (MSIT) (No. RS-2023-00209799). Portions of this work were performed under the auspices of the U.S. Department of Energy by Lawrence Livermore National Laboratory under Contract DE-AC52-07NA27344.

**Data Availability** The data that support the findings of this study are available from the corresponding author upon reasonable request.

## Declarations

**Conflict of interest** The authors declare that they have no conflict of interest.

**Open Access** This article is licensed under a Creative Commons Attribution 4.0 International License, which permits use, sharing, adaptation, distribution and reproduction in any medium or format, as long as you give appropriate credit to the original author(s) and the source, provide a link to the Creative Commons licence, and indicate if changes were made. The images or other third party material in this article are included in the article's Creative Commons licence, unless indicated otherwise in a credit line to the material. If material is not included in the article's Creative Commons licence and your intended use is not permitted by statutory regulation or exceeds the permitted use, you will need to obtain permission directly from the copyright holder. To view a copy of this licence, visit <http://creativecommons.org/licenses/by/4.0/>.

## References

- Adams M, Sines G (1978) Crack extension from flaws in a brittle material subjected to compression. *Tectonophysics* 49(1):97–118
- Arndt D, Bangerth W, Clevenger TC, Davydov D, Fehling M, Garcia-Sanchez D, Harper G, Heister T, Heltai L, Kronbichler M, Kynch RM, Maier M, Pelteret J-P, Turcksin B, Wells D (2019) The deal. II library, version 9.1. *J Numer Math* 27(4):203–213
- Barenblatt GI (1962) The mathematical theory of equilibrium cracks in brittle fracture. *Adv Appl Mech* 7:55–129
- Bažant ZP, Kazemi MT (1990) Determination of fracture energy, process zone length and brittleness number from size effect, with application to rock and concrete. *Int J Fract* 44:111–131
- Bobet A, Einstein HH (1998a) Numerical modeling of fracture coalescence in a model rock material. *Int J Fract* 92(3):221–252
- Bobet A, Einstein HH (1998b) Fracture coalescence in rock-type materials under uniaxial and biaxial compression. *Int J Rock Mech Min Sci* 35(7):863–888
- Bombolakis EG (1968) Photoelastic study of initial stages of brittle fracture in compression. *Tectonophysics* 6(6):461–473
- Browning J, Meredith PG, Stuart C, Healy D, Harland S, Mitchell TM (2017) Acoustic characterization of crack damage evolution in sandstone deformed under conventional and true triaxial loading. *J Geophys Res Solid Earth* 122(6):4395–4412
- Bryant EC, Sun W (2018) A mixed-mode phase field fracture model in anisotropic rocks with consistent kinematics. *Comput Methods Appl Mech Eng* 342:561–584
- Cheng Y, Wong LNY, Zou C (2015) Experimental study on the formation of faults from en-echelon fractures in Carrara Marble. *Eng Geol* 195:312–326
- Choo J (2019) Stabilized mixed continuous/enriched Galerkin formulations for locally mass conservative poromechanics. *Comput Methods Appl Mech Eng* 357:112568
- Choo J, Sun W (2018a) Coupled phase-field and plasticity modeling of geological materials: from brittle fracture to ductile flow. *Comput Methods Appl Mech Eng* 330:1–32
- Choo J, Sun W (2018b) Cracking and damage from crystallization in pores: coupled chemo-hydro-mechanics and phase-field modeling. *Comput Methods Appl Mech Eng* 335:347–379
- Choo J, Semnani SJ, White JA (2021) An anisotropic viscoplasticity model for shale based on layered microstructure homogenization. *Int J Numer Anal Meth Geomech* 45(4):502–520

- Choo J, Sun Y, Fei F (2023) Size effects on the strength and cracking behavior of flawed rocks under uniaxial compression: from laboratory scale to field scale. *Acta Geotech* 18:3451–3468
- Cocco M, Rice JR (2002) Pore pressure and poroelasticity effects in coulomb stress analysis of earthquake interactions. *J Geophys Res Solid Earth* 107(B2):ESE-2
- Colmenares LB, Zoback MD (2002) A statistical evaluation of intact rock failure criteria constrained by polyaxial test data for five different rocks. *Int J Rock Mech Min Sci* 39(6):695–729
- Cotterell B (1972) Brittle fracture in compression. *Int J Fract Mech* 8(2):195–208
- da Silva Jr MN, Duda FP, Fried E (2013) Sharp-crack limit of a phase-field model for brittle fracture. *J Mech Phys Solids* 61(11):2178–2195
- Dugdale DS (1960) Yielding of steel sheets containing slits. *J Mech Phys Solids* 8(2):100–104
- Dyskin A, Sahouryeh E, Jewell R, Joer H, Ustinov K (2003) Influence of shape and locations of initial 3-D cracks on their growth in uniaxial compression. *Eng Fract Mech* 70(15):2115–2136
- Fei F, Choo J (2020a) A phase-field method for modeling cracks with frictional contact. *Int J Numer Methods Eng* 121(4):740–762
- Fei F, Choo J (2020b) A phase-field model of frictional shear fracture in geologic materials. *Comput Methods Appl Mech Eng* 369:113265
- Fei F, Choo J (2021) Double-phase-field formulation for mixed-mode fracture in rocks. *Comput Methods Appl Mech Eng* 376:113655
- Fei F, Sun Y, Wong LNY, Choo J (2021) Phase-field modeling of mixed-mode fracture in rocks with discontinuities: from laboratory scale to field scale. In: 55th US rock mechanics/geomechanics symposium, pp ARMA–21–1223
- Fei F, Choo J, Liu C, White JA (2022) Phase-field modeling of rock fractures with roughness. *Int J Numer Anal Meth Geomech* 46(5):841–868
- Geelen RJ, Liu Y, Hu T, Tupek MR, Dolbow JE (2019) A phase-field formulation for dynamic cohesive fracture. *Comput Methods Appl Mech Eng* 348:680–711
- Ha YD, Lee J, Hong J-W (2015) Fracturing patterns of rock-like materials in compression captured with peridynamics. *Eng Fract Mech* 144:176–193
- Ha SJ, Choo J, Yun TS (2018) Liquid CO<sub>2</sub> fracturing: effect of fluid permeation on the breakdown pressure and cracking behavior. *Rock Mech Rock Eng* 51:3407–3420
- Haimson B (2006) True triaxial stresses and the brittle fracture of rock. *Pure Appl Geophys* 163:1101–1130
- Haimson B, Chang C (2000) A new true triaxial cell for testing mechanical properties of rock, and its use to determine rock strength and deformability of Westerly granite. *Int J Rock Mech Min Sci* 37(1–2):285–296
- Haimson BC, Rudnicki JW (2010) The effect of the intermediate principal stress on fault formation and fault angle in siltstone. *J Struct Geol* 32(11):1701–1711
- Hoek E, Bieniawski Z (1965) Brittle fracture propagation in rock under compression. *Int J Fract Mech* 1(3):137–155
- Hou P, Su S, Liang X, Gao F, Cai C, Yang Y, Zhang Z (2021) Effect of liquid nitrogen freeze-thaw cycle on fracture toughness and energy release rate of saturated sandstone. *Eng Fract Mech* 258:108066
- Ingraffea AR, Heuze FE (1980) Finite element models for rock fracture mechanics. *Int J Numer Anal Methods Geomech* 4(1):25–43
- Kwaśniewski M (2013) Mechanical behavior of rocks under true triaxial compression conditions—a review. In: True triaxial testing of rocks. CRC Press, p 99–138
- Lee H, Jeon S (2011) An experimental and numerical study of fracture coalescence in pre-cracked specimens under uniaxial compression. *Int J Solids Struct* 48(6):979–999
- Lee J, Hong J-W, Jung J-W (2017) The mechanism of fracture coalescence in pre-cracked rock-type material with three flaws. *Eng Geol* 223:31–47
- Lu Y, Wang L, Elsworth D (2015) Uniaxial strength and failure in sandstone containing a pre-existing 3-D surface flaw. *Int J Fract* 194(1):59–79
- Lu Y, Pu H, Wang L, Li Z, Meng X, Wang B, Zhang K (2021) Fracture evolution in mudstone specimens containing a pre-existing flaw under true triaxial compression. *Int J Rock Mech Min Sci* 138:104594
- Ma X, Haimson BC (2016) Failure characteristics of two porous sandstones subjected to true triaxial stresses. *J Geophys Res Solid Earth* 121(9):6477–6498
- Ma X, Rudnicki JW, Haimson BC (2017) Failure characteristics of two porous sandstones subjected to true triaxial stresses: applied through a novel loading path. *J Geophys Res Solid Earth* 122(4):2525–2540
- Morgan SP, Johnson CA, Einstein HH (2013) Cracking processes in barre granite: fracture process zones and crack coalescence. *Int J Fract* 180(2):177–204
- Nejati M, Bahrami B, Ayatollahi MR, Driesner T (2021) On the anisotropy of shear fracture toughness in rocks. *Theor Appl Fract Mech* 113:102946
- Palmer AC, Rice JR (1973) The growth of slip surfaces in the progressive failure of over-consolidated clay. *Proc R Soc Lond A Math Phys Sci* 332(1591):527–548
- Park CH, Bobet A (2009) Crack coalescence in specimens with open and closed flaws: a comparison. *Int J Rock Mech Min Sci* 46(5):819–829
- Sagong M, Bobet A (2002) Coalescence of multiple flaws in a rock-model material in uniaxial compression. *Int J Rock Mech Min Sci* 39(2):229–241
- Sahouryeh E, Dyskin AV, Germanovich LN (2002) Crack growth under biaxial compression. *Eng Fract Mech* 69:2187–2198
- Santillán D, Juanes R, Cueto-Felgueroso L (2018) Phase field model of hydraulic fracturing in poroelastic media: fracture propagation, arrest, and branching under fluid injection and extraction. *J Geophys Res Solid Earth* 123(3):2127–2155
- Shalev E, Lyakhovsky V (2018) The role of the intermediate principal stress on the direction of damage zone during hydraulic stimulation. *Int J Rock Mech Min Sci* 107:86–93
- Shen B, Stephansson O (1994) Modification of the G-criterion for crack propagation subjected to compression. *Eng Fract Mech* 47(2):177–189
- Wang H, Dyskin A, Pasternak E, Dight P, Sarmadivaleh M (2018) Effect of the intermediate principal stress on 3-D crack growth. *Eng Fract Mech* 204:404–420
- Wiebols G, Cook N (1968) An energy criterion for the strength of rock in polyaxial compression. *Int J Rock Mech Min Sci Geomech Abstr* 5(6):529–549
- Wong LNY (2008) Crack coalescence in molded gypsum and Carrara marble. Ph.D. thesis, Massachusetts Institute of Technology
- Wong LNY, Einstein HH (2009a) Using high speed video imaging in the study of cracking processes in rock. *Geotech Test J* 32(2):164–180
- Wong LNY, Einstein HH (2009b) Crack coalescence in molded gypsum and Carrara marble: Part 1. Macroscopic observations and interpretation. *Rock Mech Rock Eng* 42(3):475–511
- Wong LNY, Einstein HH (2009c) Crack coalescence in molded gypsum and Carrara marble: part 2—microscopic observations and interpretation. *Rock Mech Rock Eng* 42(3):513–545
- Wong LNY, Einstein HH (2009d) Systematic evaluation of cracking behavior in specimens containing single flaws under uniaxial compression. *Int J Rock Mech Min Sci* 46(2):239–249
- Wu J-Y (2017) A unified phase-field theory for the mechanics of damage and quasi-brittle failure. *J Mech Phys Solids* 103:72–99

- Wu Z, Wong LNY (2012) Frictional crack initiation and propagation analysis using the numerical manifold method. *Comput Geotech* 39:38–53
- Yang S-Q, Jing H-W, Wang S-Y (2012) Experimental investigation on the strength, deformability, failure behavior and acoustic emission locations of red sandstone under triaxial compression. *Rock Mech Rock Eng* 45(4):583–606
- Yin P, Wong RHC, Chau KT (2014) Coalescence of two parallel pre-existing surface cracks in granite. *Int J Rock Mech Min Sci* 68:66–84
- Zhang X-P, Wong LNY (2013) Crack initiation, propagation and coalescence in rock-like material containing two flaws: a numerical study based on bonded-particle model approach. *Rock Mech Rock Eng* 46(5):1001–1021
- Zhang Y, Liu S, Kou M, Wang Z (2020) Mechanical and failure characteristics of fissured marble specimens under true triaxial compression: insights from 3-D numerical simulations. *Comput Geotech* 127:103785
- Zhang Y, Zhang Q-Y, Zhou X-Y, Xiang W (2021) Direct tensile tests of red sandstone under different loading rates with the self-developed centering device. *Geotech Geol Eng* 39:709–718
- Zhang J-Z, Zhou X-P, Du Y-H (2023) Cracking behaviors and acoustic emission characteristics in brittle failure of flawed sandstone: a true triaxial experiment investigation. *Rock Mech Rock Eng* 56(1):167–182
- Zhang T, Chen Q-Z, Zhang J-Z, Zhou X-P (2023b) Influences of mechanical contrast on failure characteristics of layered composite rocks under true-triaxial stresses. *Rock Mech Rock Eng* 1–19
- Zhang J, Zhou X (2022) Fracture process zone (FPZ) in quasi-brittle materials: review and new insights from flawed granite subjected to uniaxial stress. *Eng Fract Mech* 108795
- Zhou X-P, Zhang J-Z, Wong LNY (2018) Experimental Study on the growth, coalescence and wrapping behaviors of 3D cross-embedded flaws under uniaxial compression. *Rock Mech Rock Eng* 51(5):1379–1400
- Zhou X-P, Zhang J-Z, Yang S-Q, Berto F (2021a) Compression-induced crack initiation and growth in flawed rocks: a review. *Fat Fract Eng Mater Struct* 44(7):1681–1707
- Zhou X-P, Peng S-L, Zhang J-Z, Berto F (2021b) Failure characteristics of coarse and fine sandstone containing two parallel fissures subjected to true triaxial stresses. *Theor Appl Fract Mech* 112:102932

**Publisher's Note** Springer Nature remains neutral with regard to jurisdictional claims in published maps and institutional affiliations.